Lithium transport in Li$_{4.4}$*M*$_{0.4}$*M'*$_{0.6}$S$_4$ (*M*= Al^{3+}, Ga^{3+} and *M'*= Ge^{4+}, Sn^{4+}): Combined crystallographic, conductivity, solid state NMR and computational studies

Bernhard T. Leube[1], Kenneth K. Inglis[1], Elliot Carrington[1], Paul M. Sharp[1], J. Felix Shin[1], Alex R. Neale[1,2], Troy D. Manning[1], Michael J. Pitcher[1], Laurence J. Hardwick [1,2], Matthew S. Dyer[1], Frédéric Blanc[1,2], John B. Claridge[1] and Matthew J. Rosseinsky[1]

[1]Department of Chemistry, University of Liverpool, Crown Street, L69 7ZD, UK

[2]Stephenson Institute for Renewable Energy, University of Liverpool, Peach Street, L69 7ZF, UK

ABSTRACT

In order to understand the structural and compositional factors controlling lithium transport in sulfides, we explored the Li$_5$AlS$_4$ – Li$_4$GeS$_4$ phase field for new materials. Both parent compounds are defined structurally by a hexagonal close packed sulfide lattice, where distinct arrangements of tetrahedral metal sites give Li$_5$AlS$_4$ a layered structure and Li$_4$GeS$_4$ a three dimensional structure related to γ-Li$_3$PO$_4$. The combination of the two distinct structural motifs is expected to lead to new structural chemistry. We identified the new crystalline phase Li$_{4.4}$Al$_{0.4}$Ge$_{0.6}$S$_4$, and investigated the structure and Li$^+$ ion dynamics of the family of structurally related materials Li$_{4.4}$*M*$_{0.4}$*M'*$_{0.6}$S$_4$ (*M*= Al^{3+}, Ga^{3+} and *M'*= Ge^{4+}, Sn^{4+}). We used neutron diffraction to solve the full structures of the Al-homologues, which adopt a layered close-packed structure with a new arrangement of tetrahedral (*M/M'*) sites and a novel combination of ordered and disordered lithium vacancies. AC impedance spectroscopy revealed lithium conductivities in the range 3(2) x 10^{-6} to 4.3(3) x 10^{-5} S cm^{-1} at room temperature with activation energies between 0.43(1) and 0.38(1) eV. Electrochemical performance was tested in a plating and stripping experiment against Li metal electrodes and showed good stability of the Li$_{4.4}$Al$_{0.4}$Ge$_{0.6}$S$_4$ phase over 200 hours. A combination of variable temperature ^{7}Li solid state nuclear magnetic resonance spectroscopy and *ab initio* molecular dynamics calculations on selected phases showed that two dimensional diffusion with a low energy barrier of 0.17 eV is responsible for long-range lithium transport, with diffusion pathways mediated by the disordered vacancies while the ordered vacancies do not contribute to the conductivity. This new structural family of sulfide Li$^+$ ion conductors offers insight into the role of disordered vacancies on Li$^+$ ion conductivity mechanisms in hexagonally close packed sulfides that can inform future materials design.

1. INTRODUCTION

There is considerable current interest in solid state lithium ion batteries.[1-3] Solid electrolytes may reduce the safety issues associated with solvent-based electrolytes and could also offer improved operating temperature ranges, greater compatibility with new anode and cathode materials over a range of cell voltages and increased long-term cyclability. To realise these advantages, electrolyte materials with appropriate conductivities, redox stabilities to anode and cathode and the mechanical properties required for functional interfaces with both electrodes are needed, which is a significant research challenge. Progress on solid electrolyte materials have been reviewed recently.[4-9]

Many of the highest reported ambient temperature lithium conductivities in solids are found in sulfide-containing materials, associated with the ionic size and polarizability of the sulfide anion. For example, $Li_{10}GeP_2S_{12}$[10] and argyrodite-related Li_6PS_5X (X= Cl, Br, I)[11] phases have conductivities of up to 1.2 x 10^{-2} and 1.33 x 10^{-3} S cm^{-1} respectively,[12] which are comparable with conventional non-aqueous solvent-based electrolytes. Sulfur-based materials are readily cold-pressed to overcome the problem of high grain boundary resistance encountered frequently in oxide-based electrolytes,[13] but can be more prone to electrochemical compatibility problems due to the reduced redox stability of the sulfide anion. Experimental[14] and computational[15] work provide evidence for the in-operando reduction of $Li_{10}GeP_2S_{12}$ into Ge, $Ge_4Li_{15,}$ and Li_3P, and of Li_6PS_5Cl into Li_3P, Li_2S, LiCl. Recently $Li_{11}AlP_2S_{12}$ has been reported on with a conductivity of 8.02 x 10^{-4} S cm^{-1} and an excellent stability against lithium metal.[16]

The structures of many lithium-containing metal sulfides such as Li_3PS_4,[17] Li_4GeS_4,[18] Li_4SnS_4,[19] Li_2FeS_2[20] and $LiGaS_2$[21] are derived from an hexagonal closed packed sulfide array and the high valent cation occupies a tetrahedral site whilst the lithium either occupies the tetrahedral sites (*e.g.* γ-Li_3PS_4)[17] or a mixture of the octahedral and tetrahedral sites, particularly when the cation to anion ratio exceeds 1. In addition to the structure report of Li_5AlS_4, the structures of some lithium containing metal sulfides have been reviewed recently by Lim et al.[22] Here we use Li_2FeS_2 to introduce the basic structural motifs in this paper. The hcp sublattice of sulfur atoms has one octahedral site and two tetrahedral interstitial sites per sulfide anion. Tetrahedral sites can be distinguished according to their orientation along the stacking axis as T^+ and T^- sites. In Li_2FeS_2, two layers of interstitials can be distinguished according to the coordination of species occupying them, as shown Figure 1 (a)-(c). Fe1 and Li2 ions occupy all the tetrahedral sites (T^+ and T^-) in the tetrahedral layer in a disordered manner, while all octahedral interstices in this layer remain empty. This layer is alternately stacked along the c-axis with an octahedral layer with Li1 occupying all octahedral interstitial sites, while all tetrahedral sites remain empty in this layer. In total half of the octahedral sites and half of the tetrahedral sites are occupied in Li_2FeS_2. Li_5AlS_4 is closely related though it crystallises in a $P2_1/m$ (**a−b**, 2**a**+2**b**, **c**) supercell with Li and Al ordered on the tetrahedral sites (**Error! Reference source not found.** (d)-(e)). This generates two crystallographically distinct Li sites in the "octahedral" layer. One is a near-regular octahedron whereas the other has the lithium displaced from the centroid of the six sulfides giving a five coordinate environment (**Error! Reference source not found.** (f)), which can be understood on electrostatic grounds by considering the configuration of nearest neighbour cations (Figure S1). The material has a room temperature lithium ion conductivity of 10^{-9} S cm^{-1} [23] and its crystal structure is characterised by fully occupied lithium sites. Increasing carrier concentration by aliovalent doping is a common way to increase lithium mobility, and the introduction of multiple species occupying the tetrahedral sites can control the lithium distribution and available diffusion pathways. Thus exploring combinations of Li_5AlS_4 and Li_4MS_4 (*M* = Si, Ge, Sn), represents a logical attempt to increase the lithium ion conductivity. All three Li_4MS_4 phases are reported to be isostructural, crystallising in a stuffed γ-Li_3PS_4 type with common ordering of Li and *M* on the

2

tetrahedral sites and ¼ of the octahedral sites occupied in an ordered manner (**Error! Reference source not found.** (i)).[19] Kanno and co-workers have previously studied the Li_5AlS_4-Li_4SiS_4 and Li_5GaS_4-Li_4GeS_4 systems where M rich phases are reported to form an orthorhombic phase with improved conductivity though no atomic coordinates are reported.[23-24] This suggests the existence of a new structural family of sulfide-based Li^+ ion conductors.

Therefore we chose to investigate the Li_5AlS_4-Li_4GeS_4 system synthetically. We report the lithium-containing metal sulfides $Li_{4.4}M_{0.4}M'_{0.6}S_4$ (M= Al^{3+}, Ga^{3+} and M'= Ge^{4+}, Sn^{4+}) and solve and refine their crystal structures from powder X-ray and neutron diffraction data. Lithium ion transport was investigated by AC impedance spectroscopy, solid state NMR spectroscopy and *ab initio* molecular dynamics (AIMD) and the resulting two-dimensional diffusion pathways connected to the vacancy order imposed by the different tetrahedral non-lithium species in the newly observed structure.
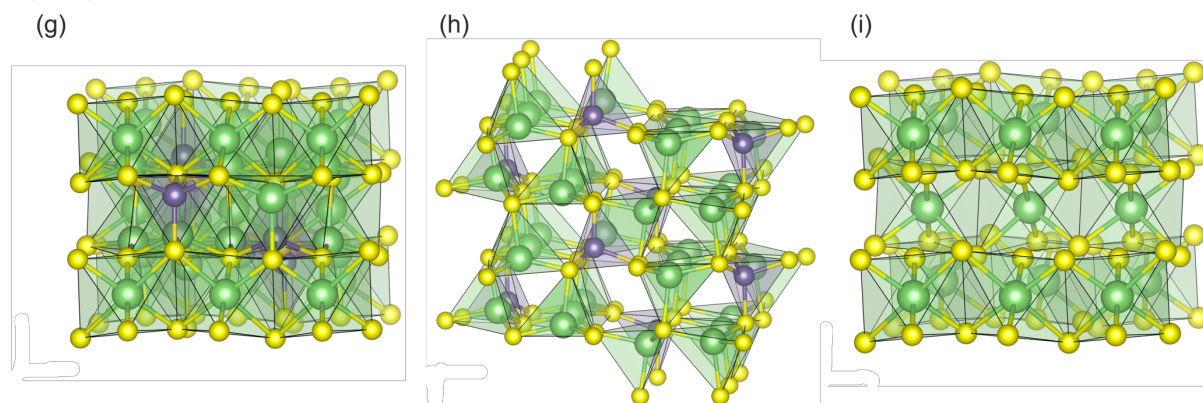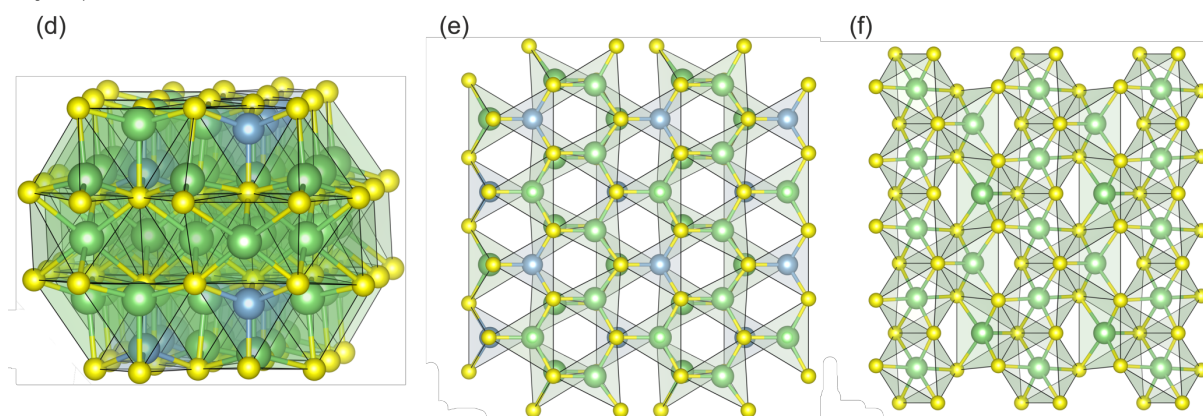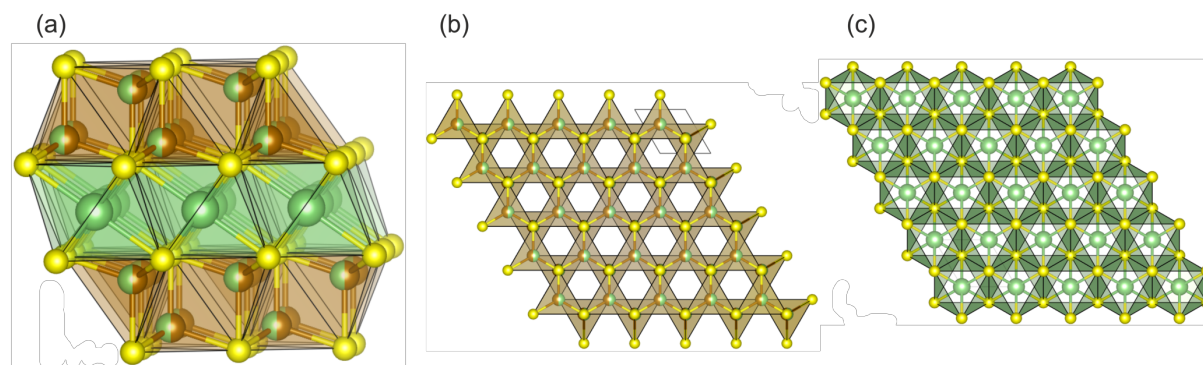
Li₂FeS₂

(a)

(b)

(c)

Li₅AlS₄

(d)

(e)

(f)

Li₄GeS₄

(g)

(h)

(i)

Figure 1: (a) Crystal structure of Li$_2$FeS$_2$ viewed along **a**. The tetrahedral layer consists of disordered mixed Li/Fe sites. (b) View of the tetrahedral layer of Li$_2$FeS$_2$ with a single tetrahedral site occupied in a disordered manner by Li and Fe along **c**. Both the T$^+$ and T$^-$ sites in the hexagonal close packed sulfide array are occupied in this layer. (c) View of the fully occupied octahedral layer of Li$_2$FeS$_2$ along **c**. (d) layered crystal structure of Li$_5$AlS$_4$ viewed along **a**. (e) View of the tetrahedral layer of Li$_5$AlS$_4$ along **c**. (f) View of the octahedral layer of Li$_5$AlS$_4$ along **c**. (g) Crystal structure of Li$_4$GeS$_4$ viewed along **a**. (h) GeS$_4$ and LiS$_4$ tetrahedra in Li$_4$GeS$_4$ forming a γ-Li$_3$PO$_4$ type coordination network viewed along **b**. (i) Net formed by the octahedral Li in Li$_4$GeS$_4$ viewed along **a**. Atoms and polyhedra are coloured as follows; brown: iron, yellow: sulfur, green: lithium, blue: aluminium and purple: germanium. Partially occupied atoms are coloured to represent fractional occupancies.

2. METHODS

2.1 Synthesis.

General procedure. All sample handling was carried out in a dry box under a helium atmosphere ($O_2 < 3$ ppm). Compositions were mixed in the appropriate stoichiometric ratio (typically in 500 mg batches), ground thoroughly and sealed as powders in evacuated carbon coated quartz tubes under a pressure of 1×10^{-4} mbar. Lithium sulfide (Li_2S, Sigma Aldrich, 99.98%, containing 3 wt% of LiOH), aluminium sulfide (Al_2S_3, Alfa Aesar, 99+%, containing Al_2S_3, with Al and S_8 as minority phases by PXRD, Figure S2), gallium sulfide (Ga_2S_3, Alfa Aesar, 99.99%), germanium powder (Alfa Aesar, 99.999%, containing 8.9 wt% GeO_2), tin sulfide, (SnS, Sigma Aldrich, $\geq$ 99.99%), phosphorous pentasulfide (P_2S_5, Sigma Aldrich, 99%) and elemental sulfur (Sigma Aldrich, 99.999%) were used as provided, unless otherwise stated. Elemental sulfur develops a high vapour pressure at elevated temperatures, therefore for all first firings the reactions were brought to 673 K at a rate of 5 K min^{-1}, then slowly heated to the final temperature at a rate of 0.3 K min^{-1}, held at the temperature, and subsequently cooled to ambient temperature at a rate of 5 K min^{-1}. When second firings were undertaken, the materials were reground, sealed in evacuated carbon coated quartz tubes as loose powders, and heated/cooled directly to the reaction temperature at a rate of 5 K min^{-1}.

Exploratory synthesis. For the initial exploration of phase formation in the Li_5AlS_4-Li_4GeS_4 phase field, the reaction mixtures were subjected to a single firing to 973 K for 12 h, with reagents used as-received.

$Li_{4.4}Al_{0.4}Ge_{0.6-x}Sn_xS_4$. To obtain high quality powder samples of $Li_{4.4}Al_{0.4}M_{0.6}S_4$ (M = Ge^{4+}, Sn^{4+}) it was necessary to reduce the Li_2S content in the initial reaction composition by 5 mol% in order to remove an Li_2S impurity phase, corresponding to a nominal stoichiometry $Li_{4.18}Al_{0.4}M_{0.6}S_{3.89}$ (M = Ge^{4+}, Sn^{4+}). This was used in all of the reactions described from here onwards, however we refer to the ICP- and Rietveld-validated "ideal" stoichiometry $Li_{4.4}Al_{0.4}M_{0.6}S_4$ for consistency of discussion. $Li_{4.4}Al_{0.4}Ge_{0.6}S_4$ and materials in the $Li_{4.4}Al_{0.4}Ge_{0.6-x}Sn_xS_4$ (x= 0, 0.2, 0.4, 0.6) series were obtained, as described in the general procedure, by heating reaction mixtures twice to 973 K for 48 h with intermediate grinding. Samples of $Li_{4.4}Al_{0.4}Ge_{0.6}S_4$ using this procedure with commercially sourced reagents were analysed by ICP elemental analysis and used in the solid state NMR data collection.

Additional samples of $Li_{4.4}Al_{0.4}Ge_{0.6}S_4$ and $Li_{4.4}Al_{0.4}Sn_{0.6}S_4$ were synthesised using in-house prepared Li_2S and purified Ge and used for synchrotron powder diffraction (SXRD) and AC-impedance experiments. Li_2S was synthesised by heating lithium carbonate (Li_2CO_3, Sigma-Aldrich, $\geq$ 99%) under a stream of CS_2 vapour to 923 K for 6 h and high purity elemental Ge was generated by heating germanium powder (Ge, Alfa Aesar, 99.999%) in 10% H_2 in argon to 873 K for 12 h to remove traces of GeO_2. To synthesise $Li_{4.4}Al_{0.4}Ge_{0.6}S_4$ and $Li_{4.4}Al_{0.4}Sn_{0.6}S_4$ reaction mixtures were fired twice to 973 K for 48 h with intermediate grinding. ICP compositional analysis and solid state NMR experiments were conducted on a sample of $Li_{4.4}Al_{0.4}Sn_{0.6}S_4$ prepared in this way.

Due to the large neutron absorption cross section of ^6Li, neutron powder diffraction (NPD) experiments were conducted on ^7Li-enriched samples of $^7Li_{4.4}Al_{0.4}Ge_{0.6}S_4$ and $^7Li_{4.4}Al_{0.4}Sn_{0.6}S_4$. ^7Li-enriched $^7Li_2S$ was synthesised by heating lithium carbonate ($^7Li_2CO_3$, Sigma-Aldrich, 99% ^7Li) under a stream of CS_2 vapour to 923 K for 6 h and used as the $^7Li_2S$ source, which was found to be phase pure by PXRD. As a one-batch synthesis at 3.5 g led to impurity phases, neutron samples were prepared by mixing a single batch of reactants and subsequently dividing this into five carbon-coated quartz tubes which were fired twice at 973 K for 48 h with intermediate grinding. After completion of the reaction, the individual products were checked for purity by PXRD yielding the same lattice parameters; the powders were combined to give in total ~ 2.5 g of ^7Li enriched samples.

Li$_{4.4}$Ga$_{0.4}$M'$_{0.6}$S$_4$. Li$_{4.4}$Ga$_{0.4}$M'$_{0.6}$S$_4$ (M'= Ge^{4+}, Sn^{4+}) phases were prepared using in-house prepared Li$_2$S and purified Ge. Reaction mixtures of the stoichiometry Li$_{4.4}$Al$_{0.4}$Ge$_{0.6}$S$_4$ were heated twice to 973 K for 24 h with intermediate grinding.

2.2 Characterisation

Compositional analysis. The composition of Li$_{4.4}$Al$_{0.4}$Sn$_{0.6}$S$_4$ was determined by measuring the lithium, aluminium and tin contents by ICP-OES (Agilent 5110 SVDV). A solution of Li$_{4.4}$Al$_{0.4}$Sn$_{0.6}$S$_4$ was prepared by dissolving 10.0 mg of sample in 4 ml aqua regia, and subsequently making up to 100 mL with deionized H$_2$O. The sulfur content could not be determined due to hydrolysis and consequent H$_2$S evolution and loss of sulfur. Elemental analysis of Li$_{4.4}$Al$_{0.4}$Ge$_{0.6}$S$_4$ was performed by Mikroanalytisches Labor Pascher at Remagen-Bandorf, Germany, after dissolution in a HF/HCl solution at elevated temperature and pressure.

X-ray powder diffraction. All powder X-ray diffraction (PXRD) experiments were carried out at ambient temperature on powders sealed in borosilicate glass capillaries under helium gas. Phase identification was carried out using Bruker D8 diffractometers with either a monochromated Mo source (Kα_1, λ = 0.7093 Å) or a monochromated Cu source (Kα_1, λ = 1.5406 Å) in Debye-Scherrer geometry. Structure determination and Rietveld refinements were carried out on synchrotron powder X-ray diffraction (SXRD) data collected from spinning capillaries (0.3mm diameter) at the I11 beamline (Diamond Light Source, UK) with an incident wavelength of 0.824878(10) Å, using the high resolution multi-analyser crystal (MAC) detectors. Variable-temperature SXRD from 100 – 500 K was carried out at I11 using an Oxford Cryostream Plus with the Mythen position sensitive detector (PSD).

Neutron powder diffraction. Time-of-flight neutron powder diffraction (NPD) data were collected on Li$_{4.4}$Al$_{0.4}$Ge$_{0.6}$S$_4$ and Li$_{4.4}$Al$_{0.4}$Sn$_{0.6}$S$_4$ using the High Resolution Powder Diffractometer (HRPD) instrument (ISIS, UK) both at 10 K and at ambient temperature. Samples were contained in thin-walled vanadium cans of diameter 6 mm, sealed with an indium gasket under 1 atmosphere of helium gas. Low temperature data were collected using an in-situ closed-cycle refrigerator (CCR). Bragg features from the CCR were manually excluded from the Rietveld refinements. Ambient-temperature data were collected with no CCR, in order to minimise background scattering. For all samples, NPD data were collected on ^{7}Li enriched samples to minimise absorption effects.

Densification. For all compositions, pellets for AC-impedance spectroscopy and stability tests against lithium metal were prepared by uniaxial pressing of ~35 mg of the powdered material in a 5mm steel die at a pressure of 2.5 MPa, followed by sintering in evacuated carbon coated quartz tubes at 923 K for 24 h. Densities in the range 75% - 82% were achieved by this method.

AC impedance spectroscopy. Temperature dependent AC-impedance spectroscopy was conducted to obtain the ionic conductivity and activation energy of each composition. Sintered pellets were painted with silver paste (RS silver conductive paint 186-3600) and dried under vacuum at ambient temperature. The measurements were performed from 303 to 398 K under argon (flow rate: 50 mL/min) using a custom-built sample holder (Figure S3) and the Solartron 1296 dielectric interface coupled with the Solartron 1255B frequency response analyser. A sinusoidal amplitude of 50 mV was employed in the frequency range 1 MHz to 100 mHz. The obtained data was analysed with the ZView2 software package (ZView2 Version: 3.5d).[25]

NMR spectroscopy. ^{6}Li, ^{27}Al and ^{119}Sn magic angle spinning (MAS) NMR spectra were recorded using a 4 mm HXY MAS Probe in double resonance mode on a 9.4 T Bruker DSX solid-state NMR spectrometer. All samples were packed in HRMAS inserts in a He glove box to eliminate air exposure.

All data acquisitions were quantitative using recycle delays longer than 5 times the spin-lattice relaxation times T_1. ^{6}Li NMR data were obtained with a pulse of length 4 μs at a radio-frequency (rf) field amplitude of 62.5 kHz and at a MAS rate of v_r = 10 kHz. ^{27}Al NMR data were all obtained with a short 30° pulse flip angle of pulse length 0.33 μs at rf amplitude of $\omega_1/2\pi(^{27}Al)$ = 83 kHz and at a MAS rate of v_r = 8 kHz. Excitation and reconversion pulses for the two dimensional z-filtered triple quantum MAS (3QMAS)[26-28] experiments were performed at rf amplitudes of $\omega_1/2\pi(^{27}Al)$ = 100 kHz and 833 Hz for the soft pulse, respectively. The ^{119}Sn NMR spectrum was obtained with a 90° pulse of pulse length 3 μs at rf amplitude of $\omega_1/2\pi(^{119}Sn)$ = 83 kHz and at a MAS rate of v_r = 10 kHz. ^{27}Al and ^{6}Li shifts were referenced to 0.1 M Al(NO$_3$)$_3$ in H$_2$O and 10 M in LiCl in D$_2$O at 0 ppm, respectively. ^{119}Sn shifts were referenced to SnO$_2$ at -604.3 ppm (equivalent to trimethyltin at 0.0 ppm).[29]

Variable temperature ^{7}Li NMR experiments were recorded on a 4 mm HXY MAS probe in double resonance mode (between 110 K – 400 K) and a 4 mm HX High Temperature MAS Probe (above room temperature), both on a 9.4 T Bruker Avance III HD spectrometer under static conditions with the X channel tuned to ^{7}Li at $\omega_0/2\pi(^7Li)$ = 156 MHz. All samples were flame sealed in Pyrex inserts under He atmosphere. All ^{7}Li NMR spectra were obtained with a hard 90° pulse of 1.5 μs at rf amplitude of $\omega_1/2\pi(^7Li)$ = 83 kHz. Spin-lattice relaxation rates in the laboratory frame (T_1^{-1}) were obtained using a saturation recovery pulse sequence and the data was fitted to a stretch exponential function of form $1 - \exp[-(\tau/T_1)^\alpha]$ where τ are the variable delays and α is the stretch exponential (values between 0.3 and 1) . Spin-lattice relaxation rates in the rotating frame ($T_{1\rho}^{-1}$) were recorded using a standard spin-lock pulse sequence at frequencies of $\omega_1/2\pi(^7Li)$ = 20, 33 and 50 kHz and data were fitted to a stretch exponential function of form $\exp[-(\tau/T_{1\rho}^{-1})^\beta]$ where β values are between 0.5 and 1. Temperature calibrations were performed using the chemical shift thermometers Pb(NO$_3$)$_2$ using ^{207}Pb NMR and CuI and CuBr using ^{63}Cu NMR.[30-33] ^{7}Li NMR shifts were referenced to 10 M LiCl in D$_2$O at 0 ppm.

Electrochemical cycling. The stabilities of Li$_{4.4}$Al$_{0.4}$Ge$_{0.6}$S$_4$ and Li$_{4.4}$Al$_{0.4}$Sn$_{0.6}$S$_4$ were tested against lithium metal electrodes. Symmetric Li|Li$_{4.4}$Al$_{0.4}$$M_{0.6}S_4$|Li cells were assembled in Swagelok-type cells using pellets of Li$_{4.4}$Al$_{0.4}$$M_{0.6}S_4$. Cells were prepared and sealed inside an Ar-filled glovebox (O$_2$; H$_2$O < 0.1 ppm). Two lithium metal disk electrodes (12 mm diameter) were punched from Li ribbon (0.38 mm thickness, Sigma Aldrich) and then mechanically pressed onto a sintered Li$_{4.4}$Al$_{0.4}$$M_{0.6}S_4$ pellet. The sealed cells were allowed to equilibrate to 323 K for 30 minutes in order to increase lithium mobility. The symmetrical cells were then cycled galvanostatically, using a VSP potentiostat/galvanostat (Biologic Science Instruments) for 100 plating and stripping cycles (J= ± 0.01 mA cm^{-2} for 1 h per half-cycle).

Plating experiment. Li|solid electrolyte|Cu asymmetrical Swagelok-type cells were likewise prepared wherein one Li disk is replaced with a 12 mm diameter Cu foil (Advent RM) disk working electrode acting as the Li deposition substrate. Prior to use, the Cu disks were soaked in 1 mol dm^{-3} HCl solution for 15 minutes, subsequently rinsed with ethanol and ultra-pure water and then dried at 373 K under vacuum. Li|SE|Cu cells were prepared and sealed inside the glovebox and then Li was deposited onto the Cu substrate under galvanostatic control for 20 h at 0.01 mA cm^{-2} (T= 323 K). The resulting cells were dismantled inside an Ar-filled glovebox and the Cu working electrode was photographed.

Ab-initio molecular dynamics simulations. Periodic, plane-wave based, density functional theory (DFT) calculations were performed using VASP[34], the PBE functional[35] and the projector augmented wave approach.[36] Calculations were performed in (**a**−**b**, 2**a**+3**b**, 2**c**) supercells of Li$_{4.4}$Al$_{0.4}$Ge$_{0.6}$S$_4$, where the supercells have a total composition of Li$_{88}$Al$_8$Ge$_{12}$S$_{80}$. Crystallographic disorder was taken into account by ranking one hundred different ordered atomic configurations within this supercell by

energy. These configurations were generated by randomly distributing atoms in the structure under the following constraints: i) each of the four tetrahedral layers within a supercell contained 2 Al and 3 Ge atoms, ii) one of the two square-pyramidal Li3 sites close to the centre of each octahedron was randomly chosen to be occupied, iii) one octahedral interstice containing Li3 sites in each of the two octahedral layers in a supercell was randomly chosen to be vacant, leading to one vacant Li3 octahedron within each half of a supercell, and iv) one quarter of the face sharing pairs of Li1 and Li2 tetrahedral sites were randomly chosen to be Li2 sites, and three quarters Li1 sites. This generates supercells where neighbouring Li1 and Li2 sites are never simultaneously occupied, and the two nearest Li3 sites are never simultaneously occupied.

The unit cell and atomic positions of the one hundred generated configurations were optimised using "fast" parameters. Reciprocal space was only sampled at the Γ point, an energy cutoff of 600 eV was used, and optimisation was completed once forces fell below 0.02 eV/Å. The configurations were ranked according to the resulting energies, and the lowest five labelled with A-E, starting with the lowest in energy (Table S1). Supercells A and B were chosen to take forward as good representative models for further study. More accurate "slow" parameters were used to reoptimise the structures of the lowest five configurations. Reciprocal space was sampled with a 3×2×3 k-point grid, and forces optimised to a tighter convergence of 0.01 eV/Å. The relative energies of supercells A–C agree well with those calculated with the "fast" parameters (Table S1). Supercell D becomes significantly more stable using the "slow" parameters, and becomes the most stable configuration. This is due to optimisation into a new configuration of cations. Subsequent optimisation using the "fast" parameters and starting from the new configuration, results in a very similar computed stability. Supercell E remains the least stable configuration. These results give us confidence that the "fast" parameters are sufficiently accurate to use for subsequent *ab initio* molecular dynamics (AIMD) calculations.

AIMD calculations were performed on supercells A and B using the "fast" parameters. A 0.5 fs time step was used throughout using the NVT ensemble. Both AIMD trajectories were initialised by performing a temperature ramp from 0 to 400 K over ~10 ps, and then an equilibration run at 400 K for ~8 ps using velocity rescaling to set the temperature. Production runs of 120 ps were performed at a set temperature of 400 K, using a Nosé thermostat, and resetting the electron density after every 8 ps.

Variations of supercell A were optimised using the "slow" parameters where one of the two Li3 vacancies was occupied by one of the surrounding Li2 atoms, in order to investigate potential Li transport pathways. This was done for each of the four Li2 atoms neighbouring one vacant Li3 site, and the two Li2 atoms neighbouring a second vacant Li3 site. For the first Li3 site, we found that all four of the Li atoms relaxed back from the Li3 site onto their original Li2 sites. It was, however, possible to stabilise Li on the second previously vacant Li3 site, defining one end of a transport pathway, with Li in the Li2 site at the other end. The barrier for the Li3 to Li2 transport along this pathway was determined by performing nudged elastic band (NEB) calculations. We used nine images constructed by placing the Li atom at equal intervals between the Li3 and Li2 positions, with the default VASP settings for the spring constant, and the "slow" parameters for optimisation.

The free energies of Li$^+$ ions along the c axes of supercells A and B were determined by placing a series of Gaussians, each centred on a Li$^+$ ion, in the supercell. All of the Gaussians had a standard deviation of 0.05 Å. For a given point along the c axis, the sum of all of the Gaussians at that point gives the density of Li$^+$ ions. The free energy is then given by $F = k_B T \ln W$, where W is the density of Li$^+$ ions and the value of T is 400K, from the AIMD calculations

3. RESULTS AND DISCUSSION

3.1 Synthesis and Structure

Exploratory synthesis was carried out along the $Li_{4+x}Al_xGe_{1-x}S_4$ tie-line between Li_5AlS_4 and Li_4GeS_4. The X-ray diffraction patterns are shown in Figure 2 and revealed that starting from the phase pure Li_4GeS_4, a new phase evolves with increasing x. In particular the region between $2\theta = 7-9°$ is indicative as a new reflection emerges at $2\theta \approx 6°$ while other reflections diminish in intensity up to x = 0.4. As x increases beyond 0.4, Li_5AlS_4 starts to form in significant quantities.
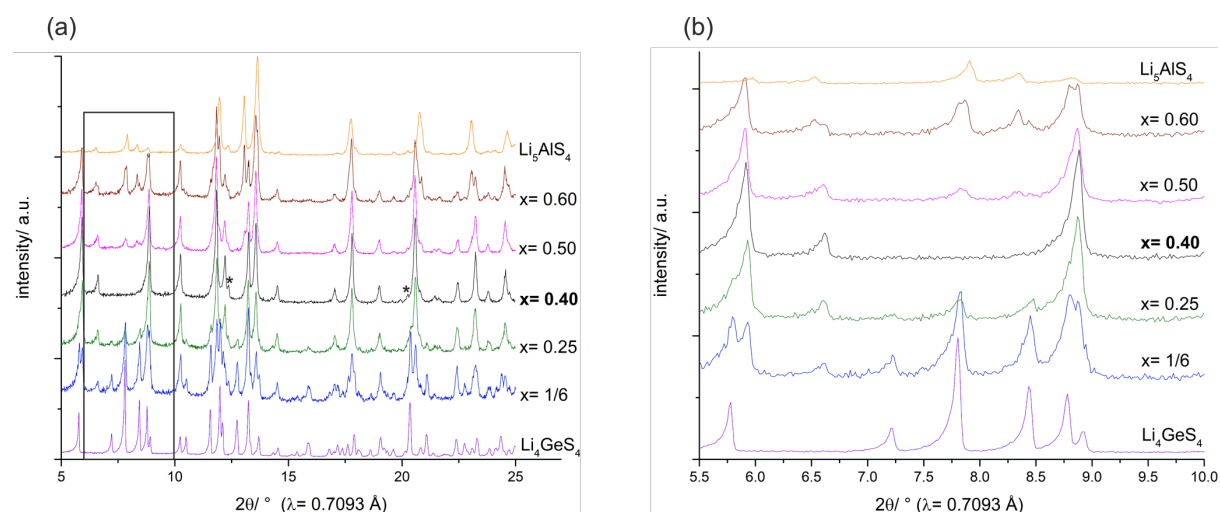
Figure 2: PXRD patterns of the $Li_{4+x}Al_xGe_{1-x}S_4$ samples along the tie line collected on a Bruker D8 diffractometer ($\lambda = 0.7093$ Å). The new crystalline phase $Li_{4.4}Al_{0.4}Ge_{0.6}S_4$ (x= 0.4) is marked in bold (Li_2S impurity phase is marked by asterisk). (a) Full pattern. (b) Magnified view of the $2\theta = 5.5-10$ ° region.

The laboratory PXRD pattern of $Li_{4.4}Al_{0.4}Ge_{0.6}S_4$ cannot be fitted satisfactorily to the end members Li_4GeS_4 or Li_5AlS_4, and contains only Li_2S as a secondary phase. Refinement of the synthesis protocol by removing 5 mol% of the initial Li_2S was successful in eliminating this Li_2S impurity, giving a new nominal reaction stoichiometry of $Li_{4.18}Al_{0.4}Ge_{0.6}S_{3.89}$. ICP-OES compositional analysis gave an overall composition of $Li_{4.40(9)}Al_{0.44(1)}Ge_{0.64(1)}S_{3.99(8)}$ (Table S2) for a sample prepared in this way, but close inspection of its SXRD pattern (Figure S4) revealed that a small quantity of Li_2S still remains (<1 wt%), in addition to Li_4GeS_4 and α-Al_2O_3 (which arises from contamination of the commercial starting materials – see Experimental), consistent with the observation of 1.97 wt% oxygen by CHNOS elemental analysis (Table S3). The ICP measurement is not sufficiently precise to distinguish between the nominal reaction stoichiometry ($Li_{4.18}Al_{0.4}Ge_{0.6}S_{3.89}$) and the ideal stoichiometry ($Li_{4.4}Al_{0.4}Ge_{0.6}S_4$) and the presence of secondary phases further complicates its interpretation: consequently, the compound is referred to as $Li_{4.4}Al_{0.4}Ge_{0.6}S_4$ hereafter. Samples prepared using in-house synthesised Li_2S and reduced Ge did not contain α-Al_2O_3, but were instead found to contain small amounts (<2 wt%) of $LiAlS_2$ and elemental Ge.

The crystal structure of $Li_{4.4}Al_{0.4}Ge_{0.6}S_4$ was solved for the heavy (non-lithium) atoms using ambient temperature synchrotron X-ray powder diffraction (SXRD) data. The SXRD pattern was provisionally indexed to an orthorhombic unit cell of similar dimensions to the Li_4GeS_4 structure but with a reduction in symmetry from *Pnma* to *Pmmm*. The precise lattice parameters were then extracted by conducting a Pawley fitting in *Pmmm*, using the unit cell parameters of Li_4GeS_4 (a = 14.03 Å, b = 7.75 Å, c = 6.15 Å) as a starting point. Simulated annealing in *P*1 symmetry using TOPAS Academic v.5 was

then used to determine the positions of the non-lithium atoms. Internal symmetry was then re-introduced by application of the FindSymm routine within Materials Studio, which transformed the annealed cells into a hexagonal setting with space group $P\bar{3}m1$. Compared to Li_2FeS_2, which adopts the same space group, the unit cell is doubled in both the **a** and **b** vectors to give a (2**a**, 2**b**, **c**) expanded cell. Rietveld refinements in this space group gave accurate positions of the metal and sulfur atoms within the asymmetric unit, with a good fit to the observed data (Figure S5). This produced a layered hcp structure, with the (Al^{3+}/Ge^{4+}) cations confined to a single layer, where they share a crystallographic site (2*d*) to exhibit ordering over a quarter of the tetrahedral interstices. The high quality of the data allowed a difference Fourier map to be implemented to give provisional, approximate Li atom positions. This suggested that the remaining tetrahedral interstices in the (Al^{3+}/Ge^{4+}) layer are populated by Li (6*i*), whilst in the second layer three quarters of the octahedral interstices are populated by Li (3*f*), which are ordered with the remaining quarter (1*b*) vacant (Figure S6).

Rietveld refinements against NPD data were conducted in GSAS[37] with low-temperature (10 K) data from $^7Li_{4.4}Al_{0.4}Ge_{0.6}S_4$ initially, in order that thermal displacement of Li ions is minimised for ease of location of additional Li sites, and for accurate refinement of their coordinates. The model derived from the SXRD structure solution provided a reasonable fit to the major features of the NPD patterns, but left several distinct mis-matches between calculated and observed intensities that could not be eliminated by refinement of atomic coordinates, occupancy parameters, or atomic displacement parameters (χ^2 = 2.76). A Fourier difference plot was generated from the high resolution backscattering bank, which revealed two lobes of negative intensity about the octahedral lithium site, corresponding to displacements of ~0.2 Å along $\bar{1}11$, and a negative peak at a second tetrahedral site, located within the "octahedral" layer, which is displaced from the starting 6*i* site by ~1 Å along 001. The structural model was modified accordingly by displacing the octahedral Li atom along $\bar{1}11$ (with its occupancy halved to compensate for the increase in multiplicity from 3*f* to 6*i*), and then by population of the additional tetrahedral Li site in the octahedral layer (6*i*), producing a model with three crystallographically independent Li atoms. This has a substantial impact on the structure, as three-quarters of the tetrahedral interstices in the "octahedral" layer are now partially occupied by lithium.

Refinement of this model eliminated the mis-matched intensities produced by the SXRD-derived structure, producing an excellent fit to the data from all three detector banks (χ^2 = 1.69, Figure 3, Table S4), with isotropic atomic displacement parameters and freely-refined Li occupancies that corresponded well to the nominal composition. The validity of this structural model at higher temperature was then tested by refinement against ambient temperature NPD data, which

produced a similarly good fit with refined Li positions and occupancies that are close to the values refined at 10 K (χ^2 = 2.04, Table S5, Figures S7-S8).
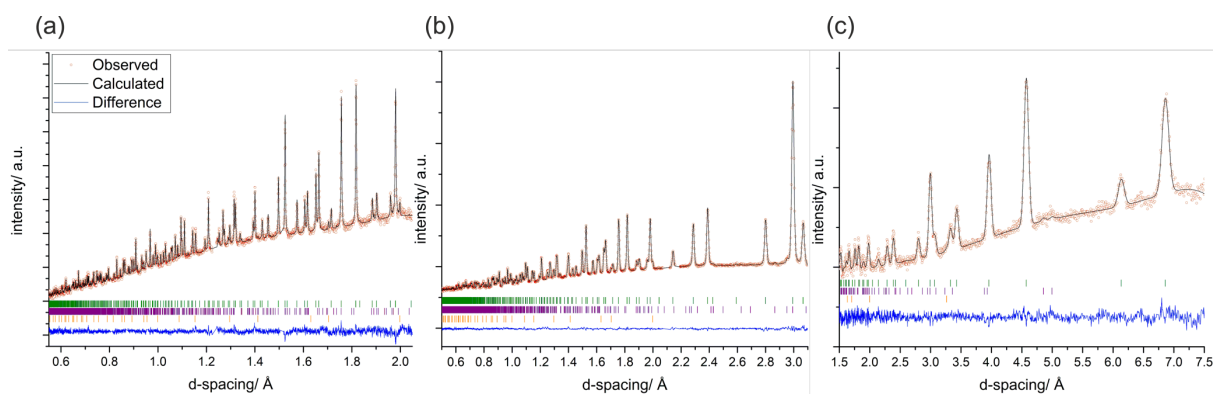

Figure 3: Rietveld refinements of $^7Li_{4.4}Al_{0.4}Ge_{0.6}S_4$ (synthesised using purified reactants) against NPD data (ISIS neutron source, HRPD line, 10 K). The positions of calculated Bragg reflections are shown by tick marks (green: $Li_{4.4}Al_{0.4}Ge_{0.6}S_4$, purple: $LiAlS_2$, orange: Ge). (a) Bank 1, 2θ = 168.3°, (b) Bank 2, 2θ = 89.6° and (c) Bank 3, 2θ = 30.0°. Note that all data banks contain a significant background contribution from the closed-cycle refrigerator sample environment.

(a) Li$_{4.4}$Al$_{0.4}$Ge$_{0.6}$S$_4$

Li1
Li2
Li3
Li3
Li2
Li1

(b)

(c)

(d) Li$_5$AlS$_4$
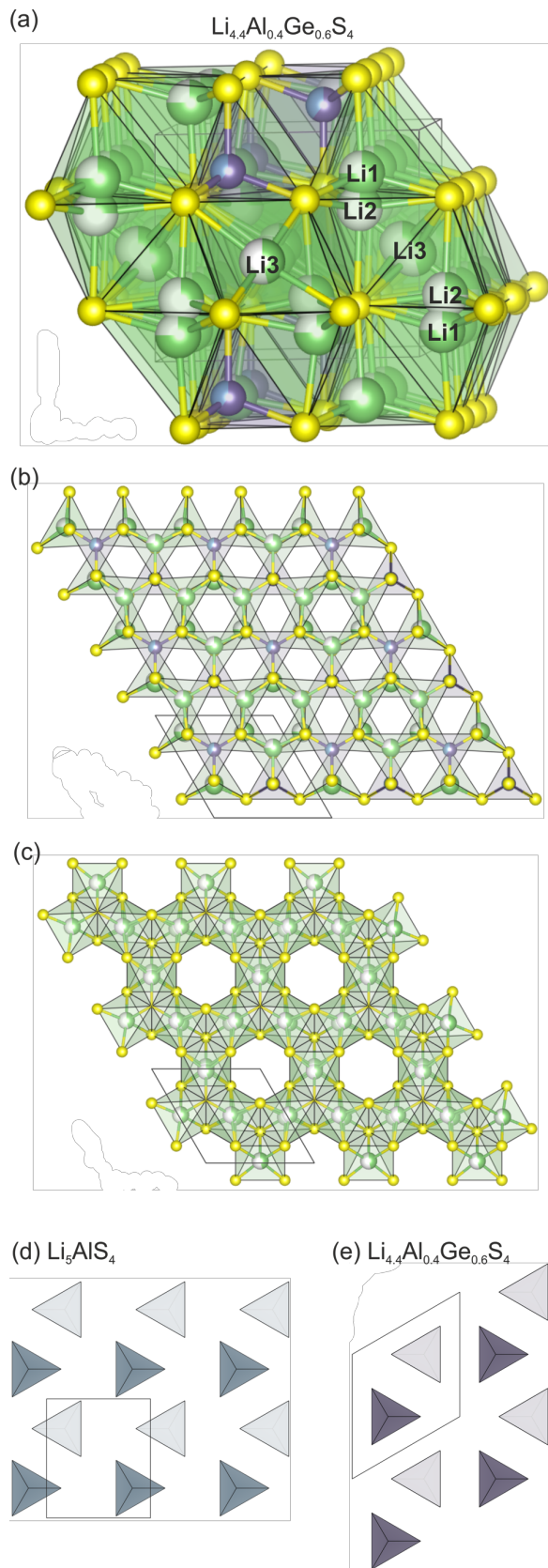
(e) Li$_{4.4}$Al$_{0.4}$Ge$_{0.6}$S$_4$

Figure 4: (a) Refined crystal structure of Li$_{4.4}$Al$_{0.4}$Ge$_{0.6}$S$_4$ at 10 K viewed perpendicular to the stacking direction. (b) View of the tetrahedral layer of Li$_{4.4}$Al$_{0.4}$Ge$_{0.6}$S$_4$ along the *c* axis illustrating the ordering of the fully-occupied mixed (Al^{3+}/Ge^{4+}) site and the partially-occupied Li1 site. (c) View of octahedral layer of Li$_{4.4}$Al$_{0.4}$Ge$_{0.6}$S$_4$ along the *c* axis, illustrating the 3:1 ordering of the lithium-occupied sites with vacant sites. Yellow: sulfur, green: lithium, blue-purple: mixed Al^{3+}/Ge^{4+} site. (d)

12

Arrangement of AlS$_4$ tetrahedra in Li$_5$AlS$_4$, viewed along the stacking axis. (e) Arrangement of MS$_4$ tetrahedra in the tetrahedral layer of Li$_{4.4}$Al$_{0.4}$Ge$_{0.6}$S$_4$ for comparison.

The final refined structure of Li$_{4.4}$Al$_{0.4}$Ge$_{0.6}$S$_4$ crystallises in the trigonal space group $P\bar{3}m1$ with two formula units per unit cell (Figure 4a). The tetrahedral layer hosts fully occupied (Al^{3+}/Ge^{4+}) sites and partially occupied Li$^+$ sites (Li1) in a 1:3 ratio. The ordering of these sites causes the (2**a**, 2**b**, **c**) expansion of the unit cell compared to that of Li$_2$FeS$_2$, with the Al^{3+}/Ge^{4+} tetrahedra ordered onto the one combination of T$^+$ and T$^-$ sites which avoids edge sharing, thus maximising the distance between the most highly charged cations. Therefore, each Al^{3+}/Ge^{4+} tetrahedron shares edges only with the three adjacent Li1 tetrahedra, as displayed in Figure 4b. The refined occupancy of the Li1 tetrahedron is 0.738(5). The remaining 0.254(4) Li occupy the Li2 tetrahedral site in the octahedral layer, which shares a face with the Li1 site (Figure 4a and Figure 6a). Li1 and Li2 have a combined occupancy of 0.992(6), which is consistent with the idea of a single lithium ion disordered over two sites in two neighbouring layers: their proximity precludes simultaneous occupancy.

In contrast to the Li$_2$FeS$_2$ structure where all of the octahedral sites in the octahedral layer are occupied, in Li$_{4.4}$Al$_{0.4}$Ge$_{0.6}$S$_4$ every fourth octahedron remains vacant and the vacancies are ordered (see Figure 4c). This octahedral vacancy ordering is coupled to the ordering of tetrahedral sites, allowing tetrahedral cations of low charge (*i.e.* Li1) to share edges or faces with vacant octahedra in adjacent layers, whilst the highly charged (Al^{3+}/Ge^{4+}) sites lie furthest away and are linked to octahedral vacancies by corner sharing (Figure 6b). Consequently, the Al^{3+}/Ge^{4+} tetrahedra share three edges and one corner with the occupied Li3 octahedral sites.

In contrast to the occupied octahedral sites in Li$_4$GeS$_4$, in Li$_{4.4}$Al$_{0.4}$Ge$_{0.6}$S$_4$ Li3 is not situated at the centroid of the octahedron. Instead, the scattering from this octahedral site is split into two symmetrical equivalents by displacement towards the S2 vertices, producing a pseudo-square-pyramidal coordination environment with four equatorial Li3-S1 bonds in the range 2.614(6) – 2.672(5) Å, one short axial Li3-S2 bond of 2.634(6) Å, and one long axial Li3-S2 bond of 3.035(6) Å (Figure 5a). Whilst this avoids the need for two long Li-S bonds (which would be required if the centroid of the octahedron were to be occupied, producing 4x 2.636(1) and 2x 2.835(1) Å Li-S distances), the displacement is not due to simple size effects. This can be seen in the bond valence sum (BVS) of 0.91 for lithium at the centroid of the octahedron, which lies between the BVS values for octahedral lithium found in Li$_5$AlS$_4$ (0.85) and Li$_4$GeS$_4$ (0.94),[18] and which increases by less than 0.01 with the observed displacement. Instead, it is the disorder of the neighbouring tetrahedral lithium sites in the same layer (Li2) that creates an electrostatic driving force for the non-centric displacement of Li3: in Li$_{4.4}$Al$_{0.4}$Ge$_{0.6}$S$_4$ the four face-sharing tetrahedral Li2 sites have an occupancy of 0.254(4), and the distance from Li2 to the centroid of the octahedron is of the order of a Li-S bond (2.527(6) Å). Consequently, the most common local configuration features an octahedron neighboured by a single occupied face-sharing Li2 tetrahedron. In this configuration, Li3 is repelled electrostatically from the shared face, driving it from the centroid of the octahedron. This approximates to the Li3 site splitting in our structural model, which provides a good fit to the observed Bragg scattering. In contrast, Li$_5$AlS$_4$ and Li$_4$GeS$_4$ feature lithium sites in a fully centric octahedral coordination because the adjacent tetrahedral sites (in the edge-sharing neighbouring layer in Li$_5$AlS$_4$, and with edge- and face-sharing in Li$_4$GeS$_4$) fully occupied to produce centrosymmetric arrangements locally.
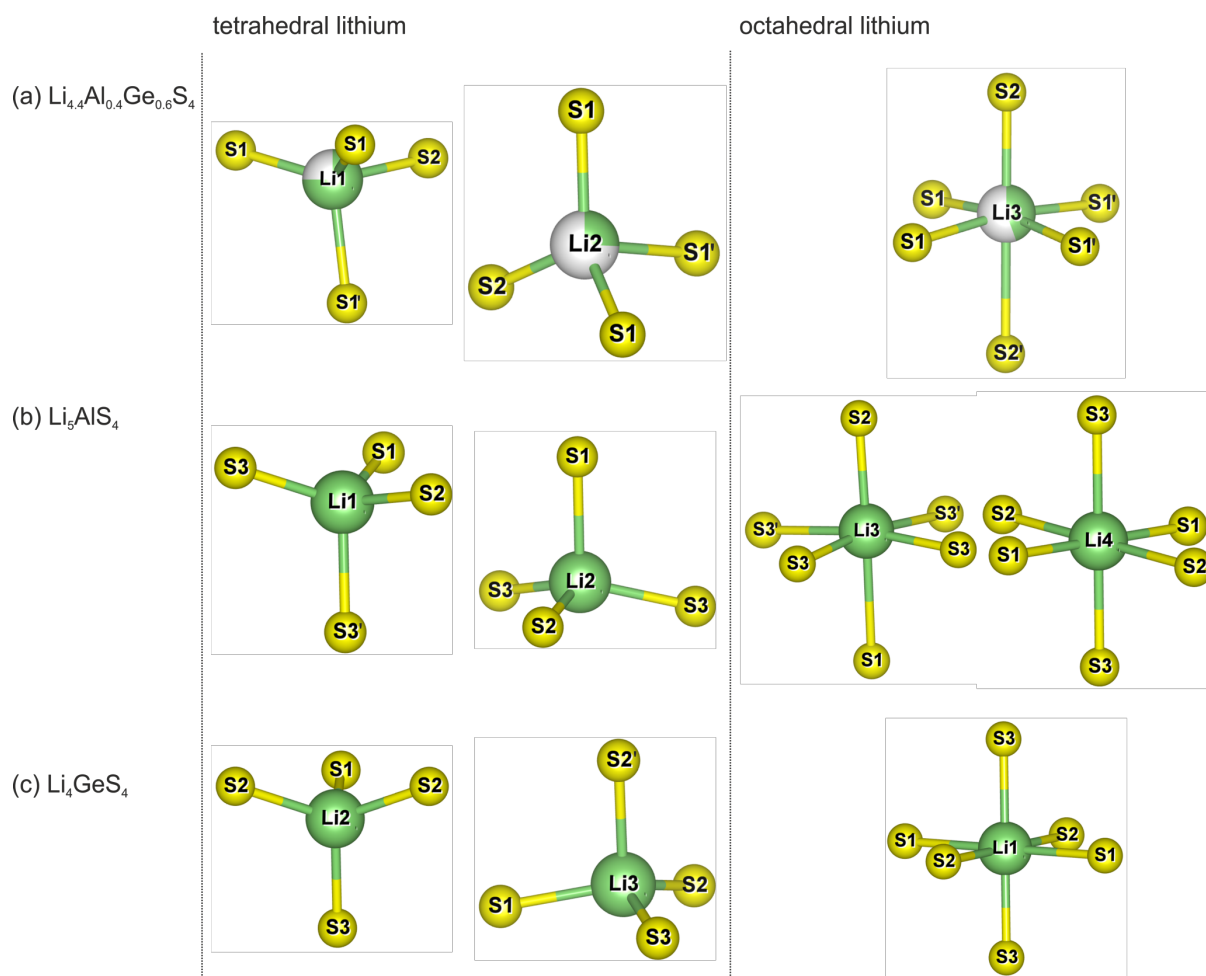
Figure 5: (a) Local lithium coordination geometries for $Li_4Al_{0.4}Ge_{0.6}S_4$ (determined at 10 K) with two tetrahedral sites (Li1 and Li2) and Li3 in octahedral/pseudo-square-pyramidal coordination geometry. (b) Local lithium coordination geometries in Li_5AlS_4 with two tetrahedral lithium sites (Li1 and Li2) two lithium sites in the octahedral layer (Li3 and Li4). (c) Local lithium coordination geometries in Li_4GeS_4 with an undistorted octahedral site (Li1) and two tetrahedral lithium sites (Li2 and Li3).
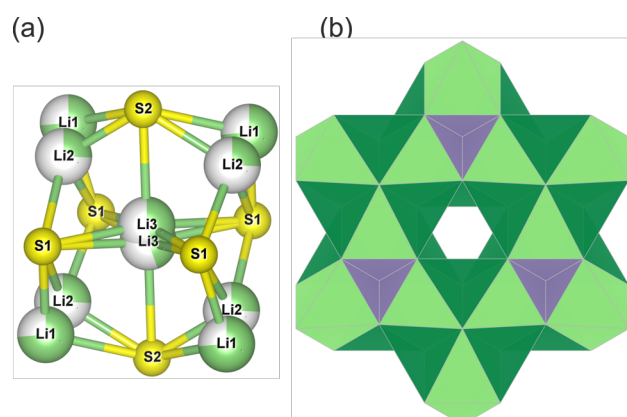
Figure 6: (a) Average arrangement of partially-occupied nearest-neighbour tetrahedral lithium ions about the octahedral Li3 sites, showing Li2 sites coordinated to four octahedral faces and Li1 coordinated to four octahedral edges, with the Li3 site split by displacement from the octahedral centroid due to the dominance of non-centrosymmetric local configurations. (b) View of the octahedral layer in $Li_4Al_{0.4}Ge_{0.6}S_4$ along **c** showing the ordering of mixed Al^{3+}/Ge^{4+} tetrahedra (purple) which are corner-linked to the empty octahedral sites (centre). Note that the partially occupied Li2 (dark green) tetrahedra in the octahedral layer share faces with both empty and occupied (light green) octahedral sites.

14

Compared to Li_2FeS_2 and Li_5AlS_4, $Li_{4.4}Al_{0.4}Ge_{0.6}S_4$ has a reduced metal:sulfur content of 5.4:4 per formula unit, and this deviation from 6:4 stoichiometry is facilitated by changes in occupancy in the octahedral layer. Per unit cell ($Li_{8.8}Al_{0.8}Ge_{1.2}S_8$) there is one ordered lithium vacancy for every three occupied lithium in the octahedral layer, which accounts for the majority of this difference, and 0.067 disordered vacancies per occupied octahedron (Figure 4c) which accounts for the remainder. In total this reduces the Li content in the octahedral layer by a total of 1.2 per unit cell (0.6 per formula unit) to preserve charge neutrality. The refined occupancies of the individual lithium sites are listed in Table 1.

Table 1: Refined occupancies of the three different lithium sites in $Li_{4.4}Al_{0.4}Ge_{0.6}S_4$ and $Li_{4.4}Al_{0.4}Sn_{0.6}S_4$ at 10 K and ambient temperature respectively.

	T/ K	occ. Li1	occ. Li2	occ. Li3
$Li_{4.4}Al_{0.4}Ge_{0.6}S_4$	10	0.738(5)	0.254(4)	0.441(7)
$Li_{4.4}Al_{0.4}Ge_{0.6}S_4$	298	0.767(6)	0.221(5)	0.461(5)
$Li_{4.4}Al_{0.4}Sn_{0.6}S_4$	10	0.575(4)	0.422(4)	0.435(7)
$Li_{4.4}Al_{0.4}Sn_{0.6}S_4$	298	0.584(4)	0.427(3)	0.460(5)

The PXRD pattern of $Li_{4.4}Al_{0.4}Ge_{0.6}S_4$ strongly resembles that of $Li_{4.25}Ga_{0.25}Ge_{0.75}S_4$ reported by Kanno et al.[24] Taking this lead that the $Li_{4.4}Al_{0.4}Ge_{0.6}S_4$ phase might be part of a larger structural family, the composition $Li_{4.4}M_{0.4}M'_{0.6}S_4$ was used as a starting point for the introduction of further cations with $M = Al^{3+}$, Ga^{3+} and $M' = Ge^{4+}$, Sn^{4+}. As with $Li_{4.4}Al_{0.4}Ge_{0.6}S_4$, no compounds were found in the Li-Al-Sn-S phase diagram by a search of the CAS Registry, and the ICSD and Pearson structural databases.

A solid solution $Li_{4.4}Al_{0.4}Ge_{0.6-x}Sn_xS_4$ was found to follow Vegard's law with unit cell parameters that expand linearly with increasing x (Figure 7), and no indication of a structural transition. ICP analysis of the $Li_{4.4}Al_{0.4}Sn_{0.6}S_4$ end member gave a metal composition of $Li_{4.40(4)}Al_{0.43(1)}Sn_{0.60(2)}$. This composition is in good agreement with $Li_{4.4}Al_{0.4}Sn_{0.6}S_4$ and will be referred to as such hereafter (see Table S6). These samples appeared single phase by laboratory PXRD, however a small amount of $LiAlS_2$ was detected by SXRD, and the NPD patterns contained a weak set of reflections (< 3% intensity of the most intense $Li_{4.4}Al_{0.4}Sn_{0.6}S_4$ peak) from an additional phase that indexed to a face centred cubic cell with $a \approx 3.95$ Å. As we could not assign a known phase to these peaks they were excluded from the Rietveld analysis.

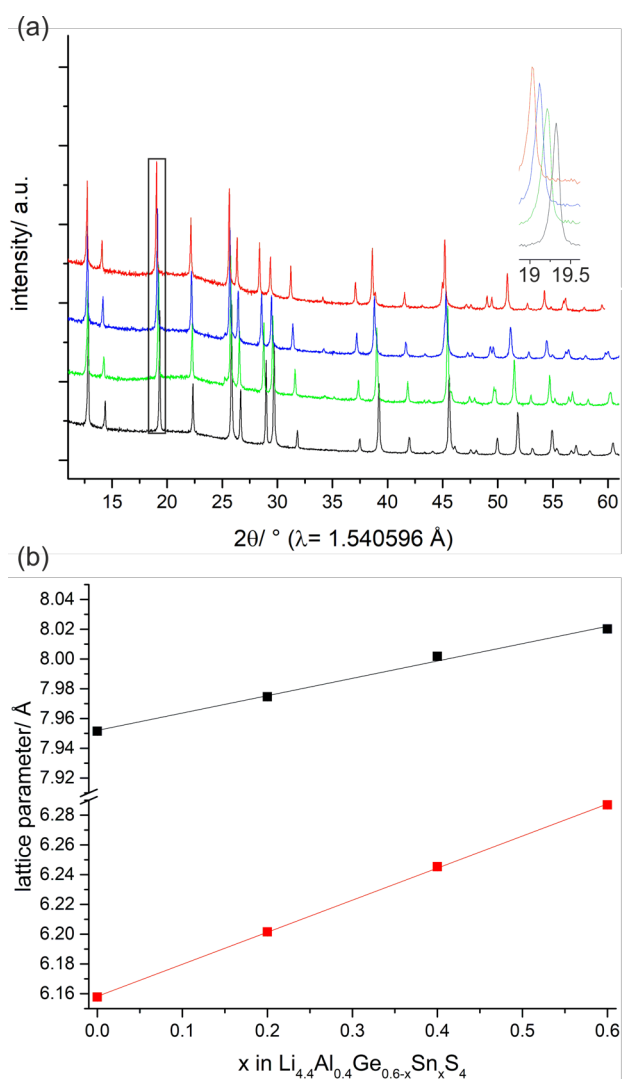Figure 7: (a) PXRD patterns of the solid solution $Li_{4.4}Al_{0.4}Ge_{0.6-x}Sn_xS_4$ (black: x= 0, green: x= 0.2, blue: x= 0.4, red: x= 0.6); inset: Close up view of the 110 reflection which continually shifts towards higher d-spacing with increasing x. (b) Lattice parameters a (black) and c (red) in the solid solution $Li_{4.4}Al_{0.4}Ge_{0.6-x}Sn_xS_4$.

The structure of $Li_{4.4}Al_{0.4}Sn_{0.6}S_4$ was refined as isostructural to $Li_{4.4}Al_{0.4}Ge_{0.6}S_4$ by X-ray and neutron powder diffraction (Figures S9-S11, Tables S7-S8). The replacement of Ge by Sn expands the hcp sulfide lattice, producing new S1-S1 distances of 3.767(1) Å and S1-S2 distances of 3.808(3) Å (compared to 3.6016(9) Å and 3.768(3) Å respectively in $Li_{4.4}Al_{0.4}Ge_{0.6}S_4$). The distribution of the lithium ions between the tetrahedral Li1 and Li2 sites changes significantly: the occupancy of Li1 decreases from 0.738(5) to 0.577(4) as more of the tetrahedral lithium ions are displaced from the tetrahedral layer into the face sharing tetrahedral Li2 site, whose occupancy increases from 0.254(4) to 0.424(4) to retain an overall occupancy of 1 between the Li1/Li2 sites. This occurs together with an exaggeration of the square-pyramidal coordination of Li3, whose displacement from the octahedral centroid is amplified from 0.202(3) to 0.259(6) Å, which reflects the coupling of Li2 occupancy and Li3 displacement discussed earlier in the context of $Li_{4.4}Al_{0.4}Ge_{0.6}S_4$. Detailed information on bond length and coordination spheres of metal and lithium sites in $Li_{4.4}Al_{0.4}Ge_{0.6}S_4$, $Li_{4.4}Al_{0.4}Sn_{0.6}S_4$, Li_5AlS_4 and Li_4GeS_4 is contained within Tables S9-S12. Raising the temperature to room temperature does not change the crystal structure or the distribution of lithium atoms significantly in either $Li_{4.4}Al_{0.4}Ge_{0.6}S_4$ or $Li_{4.4}Al_{0.4}Sn_{0.6}S_4$ phases (Table S5 and Table S8).

Table 2: Lattice parameters of the $Li_{4.4}M_{0.4}M'_{0.6}S_4$ phases with M = Al^{3+}, Ga^{3+} and M' = Ge^{4+}, Sn^{4+} obtained by Rietveld refinement of SXRD data.

	Space group	a/ Å	c/ Å	Impurity phase
$^7Li_{4.4}Al_{0.4}Ge_{0.6}S_4$*	$P\bar{3}m1$	7.9496(3)	6.1566(3)	$LiAlS_2$ (2.0 wt%), Ge (0.4 wt%)
$^7Li_{4.4}Al_{0.4}Sn_{0.6}S_4$*	$P\bar{3}m1$	8.0184(2)	6.2856(2)	$LiAlS_2$ (1.5 wt%)
$Li_{4.4}Ga_{0.4}Ge_{0.6}S_4$	$P\bar{3}m1$	7.94866(6)	6.1521(2)	-
$Li_{4.4}Ga_{0.4}Sn_{0.6}S_4$	$P\bar{3}m1$	8.0296(8)	6.2851(7)	$LiGaS_2$ (3.5 wt%)

* Samples have been synthesised with a stoichiometry of the reactants of $^7Li_{4.18}Al_{0.4}M_{0.6}S_{3.89}$.

Further cation substitution yielded $Li_{4.4}Ga_{0.4}Ge_{0.6}S_4$ and $Li_{4.4}Ga_{0.6}Sn_{0.6}S_4$. Table 2 gives an overview of crystallographic data on the four new $Li_{4.4}M_{0.4}M'_{0.6}S_4$ phases. All SXRD patterns can be indexed in the $P\bar{3}m1$ space group. Partial Rietveld refinements were carried out using SXRD data on $Li_{4.4}M_{0.4}M'_{0.6}S_4$ (M= Ga^{3+} and M'= Ge^{4+}, Sn^{4+}) to investigate any changes in the frameworks of the respective compositions. As no neutron diffraction data were available for complete structure solution only lattice parameters, positions of heavy atoms and thermal parameters were refined with Li atoms excluded from the models (Figures S13-S14, Tables S12-S13), confirming that the frameworks of these compounds are isostructural to the completely solved $Li_{4.4}Al_{0.4}Ge_{0.6}S_4$ phase. This analysis, and the key structural features that were not captured by our initial SXRD refinement of $Li_{4.4}Al_{0.4}Ge_{0.6}S_4$, both highlight the value of neutron scattering methods in obtaining accurate atomic coordinates and fractional occupancies for lithium in these systems. We note that few systems in this structural family have been characterised in this way, with Li_4GeS_4[18] and Li_5AlS_4[22] standing alongside several $Li_{10}GeP_2S_{12}$ derivatives[38-40] as the only current examples in the ICSD or Pearson databases.

3.2 Characterisation

3.2.1 AC Impedance

The ionic conductivities of $Li_{4.4}Al_{0.4}Ge_{0.6}S_4$ and $Li_{4.4}Al_{0.4}Sn_{0.6}S_4$ were determined by AC impedance spectroscopy on samples with relative densities from 75 to 82%. The typical Nyquist plots for the samples measured in flowing argon are given in Figure 8 (a) and comprise a single semicircle at high frequencies and a spike in the low frequency region. The low frequency spike is associated with the ion blocking electrode response, which is modelled with a constant phase element (CPE).[41] For $Li_{4.4}Al_{0.4}Ge_{0.6}S_4$ the capacitance value for the semicircle was obtained by fitting to an equivalent circuit model consisting of a single resistor and a CPE in parallel, which is to describe the non-idealities of the samples for this type of materials.[41] This gave a value of 8.68 x 10^{-10} F cm^{-1}, corresponding to a relative permittivity ε_R= 9803, which is too large for a bulk response alone (Table S15).

While the complex plane plot is dominated by the most resistive element, the imaginary component of the electric modulus M'' plot is dominated by the element having smaller capacitance. Since the capacitance of a bulk process is much smaller than that of a grain boundary, it is easier to identify an element associated with bulk conduction using an M'' plot. In those plots, no further peaks are identified, which indicates that the semicircle in the complex plane plot is the combination of bulk and grain boundary conduction (Figure S14(a)). The difficulty of convolution of two typical conducting elements has been expressed many times for this type of material.[23] [42] Thus we report total conductivity σ_{total} of the samples here. Nyquist plots from the full frequency range (1MHz-100mHz) are given for both compounds in Figure S14(b).
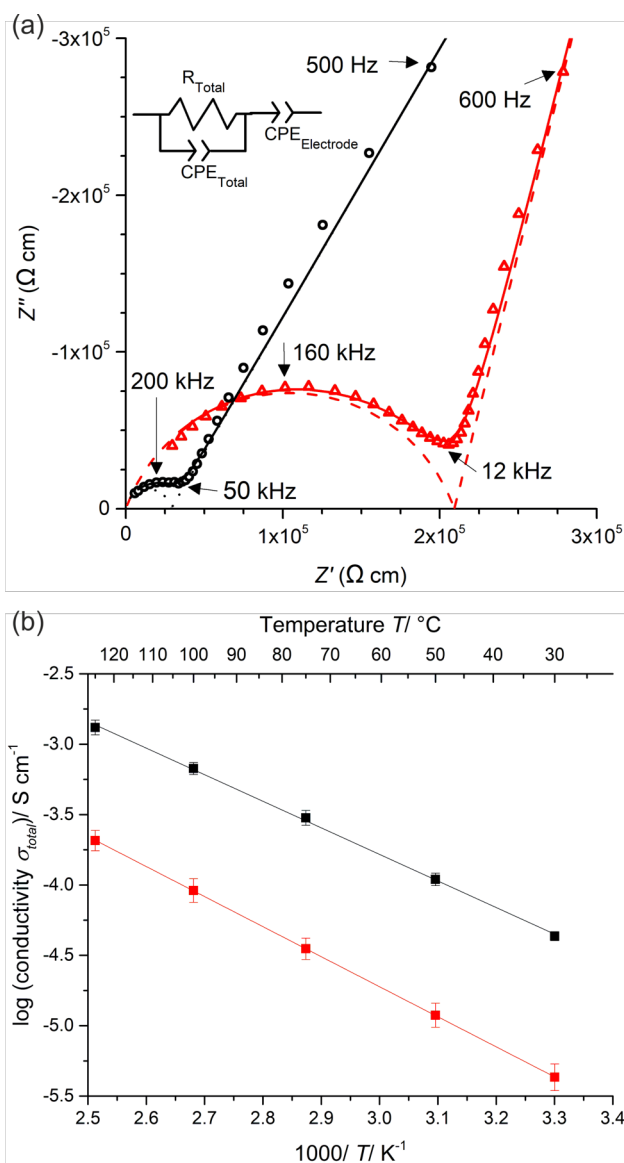
Figure 8: (a) complex plane impedance plots for $Li_{4.4}Al_{0.4}Ge_{0.6}S_4$ (black circles) and $Li_{4.4}Al_{0.4}Sn_{0.6}S_4$ (red triangles) at 303 K along with equivalent circuit model (inset); the dashed lines give the contribution of the individual components of the equivalent circuit while the solid line depicts the calculated values for the complete equivalent circuit (b) Arrhenius plots of $Li_{4.4}Al_{0.4}Ge_{0.6}S_4$ (black) and $Li_{4.4}Al_{0.4}Sn_{0.6}S_4$ (red).

The conductivity data behave according to the Arrhenius law over the measured temperature range, thus the activation energy can be estimated as given in Figure 8 (b). Table 3 gives an overview of the obtained total conductivities σ_{total} for the reported phases here and selected comparator materials.

Table 3: Conductivities and activation energies of $Li_{4.4}M_{0.4}M'_{0.6}S_4$ (M= Al^{3+}, Ga^{3+} and M'= Ge^{4+}, Sn^{4+}) and comparator materials obtained by AC-impedance spectroscopy and NMR spectroscopy.

Material	σ_{total} / S cm^{-1} (303 K)	E_a/ eV	Method	Ref
$Li_{4.4}Al_{0.4}Ge_{0.6}S_4$	4.3(3) x 10^{-5}	0.38(1)	AC Impedance	This work
	1.9(1) x 10^{-5}	0.14(2)	NMR	This work
$Li_{4.4}Al_{0.4}Sn_{0.6}S_4$	4.3(9) x 10^{-6}	0.42(1)	AC Impedance	This work
	3.6(4) x 10^{-6}	0.15(3)	NMR	This work
$Li_{4.4}Ga_{0.4}Ge_{0.6}S_4$	1.6(3) x 10^{-5}	0.40(1)	AC Impedance	This work
$Li_{4.4}Ga_{0.4}Sn_{0.6}S_4$	3(2)x10^{-6}	0.43(1)	AC Impedance	This work
$Li_{4.275}Ga_{0.25}Ge_{0.61}S_4$	6.5 x 10^{-5} (298 K)	0.46	AC-impedance	[24]
$Li_{4.8}Al_{0.8}Si_{0.2}S_4$	2.3x10^{-7}	50.3	AC-impedance	[23]
Li_4GeS_4	2 x 10^{-7} (298 K)	0.54	AC-impedance	[24]
Li_4SnS_4	7 x 10^{-5} (293 K)	0.41	AC-impedance	[43]
		0.33	NMR	[43]
Li_5AlS_4	9.7 x 10^{-9} (323 K)	0.61	AC-impedance	[22]
Li_5GaS_4	5.1 x 10^{-8} (373 K)	-	AC-impedance	[24]

Conductivities ranging from 3(2) x 10^{-6} S cm^{-1} to 4.3(3) x 10^{-5} S cm^{-1} at 303 K and activation energies from 0.43 eV to 0.38 eV have been determined with $Li_{4.4}Ga_{0.4}Sn_{0.6}S_4$ being the least and $Li_{4.4}Al_{0.4}Ge_{0.6}S_4$ being the most conducting. All materials are significantly better conductors than the respective $Li_5M^{3+}S_4$ parent phases and Li_4GeS_4, and are generally comparable to Li_4SnS_4.[43]

3.2.2 Electrochemical stability

The cyclabilities and stabilities of $Li_{4.4}Al_{0.4}Ge_{0.6}S_4$ and $Li_{4.4}Al_{0.4}Sn_{0.6}S_4$ were investigated against lithium metal electrodes at 323 K in galvanostatic plating and stripping experiments. The change in overpotential was used as a proxy for the reactions at the Li|SE interface indicating stable or unstable interfaces. All cells were cycled for more than 200 hours and, at the low current density of ±0.01 mA cm^{-2}, both electrolytes showed relatively large plating/stripping voltage plateaus (*ca*. 0.1-0.8 V) due to their low intrinsic Li conductivities (for comparison, plating/stripping of Li from $Li_{11}AlP_2S_{12}$ occurs as low as 6.3 mV in symmetrical Li cells at room temperature with even larger current densities).[16] However, the change of overpotential was found to differ significantly from one solid-state electrolyte to the other (Figure 9). The cell polarisation for the $Li_{4.4}Al_{0.4}Sn_{0.6}S_4$ electrolyte increased continuously over the 200 h cycling period, indicative of continued degradation processes occurring at the Li|SE interface. Conversely, the plating/stripping potentials observed with the $Li_{4.4}Al_{0.4}Ge_{0.6}S_4$ electrolyte stabilised after 100 h. The relative percentage increase of overpotential between 150 h and 200 h for $Li_{4.4}Al_{0.4}Ge_{0.6}S_4$ and $Li_{4.4}Al_{0.4}Sn_{0.6}S_4$ are 1% (3 mV) and 22% (170 mV), respectively. SXRD patterns of all samples were measured after completion of the plating and stripping experiment, but no significant changes in the patterns could be observed (Figure S15), confirming that the changes in overpotential were not due to major bulk degradation processes.

To validate the electrodeposition of Li^0 from the SE materials, asymmetric Li|SE|Cu cells were prepared wherein a Cu foil working electrode acts as the substrate for plating. The least-stable electrolyte, $Li_{4.4}Al_{0.4}Sn_{0.6}S_4$, showed rapid polarisation and failure, whereas the $Li_{4.4}Al_{0.4}Ge_{0.6}S_4$ electrolyte exhibited more consistent plating voltages of -0.4 to -0.6 V *vs*. Li$^+$/Li. Following deposition, the $Li_{4.4}Al_{0.4}Ge_{0.6}S_4$ cell was deconstructed inside an Ar-filled glovebox for visual inspection. A photograph of the Cu substrate (Figure S16) shows the presence of a deposited Li metal layer on the Cu surface.

These results illustrate that $Li_{4.4}Al_{0.4}Ge_{0.6}S_4$ and $Li_{4.4}Al_{0.4}Sn_{0.6}S_4$ could in principle function as Li^+ conducting electrolytes in solid-state battery devices. While the ionic conductivities of both materials are too low for practical application, the degradation/stabilisation characteristics of $Li_{4.4}Al_{0.4}Ge_{0.6}S_4$ suggest that Li^+ conductors in (or close to) the Li-Al-Ge-S phase field could offer good stability at the interface with Li-metal anodes. Conversely, the inferred degradation of the Li|SE interface with the $Li_{4.4}Al_{0.4}Sn_{0.6}S_4$ electrolyte indicates this material is incompatible in direct contact with Li-metal, which is a common barrier to practical applications even for high-performance sulfides such as $Li_{10}GeP_2S_{12}$.[14, 44]
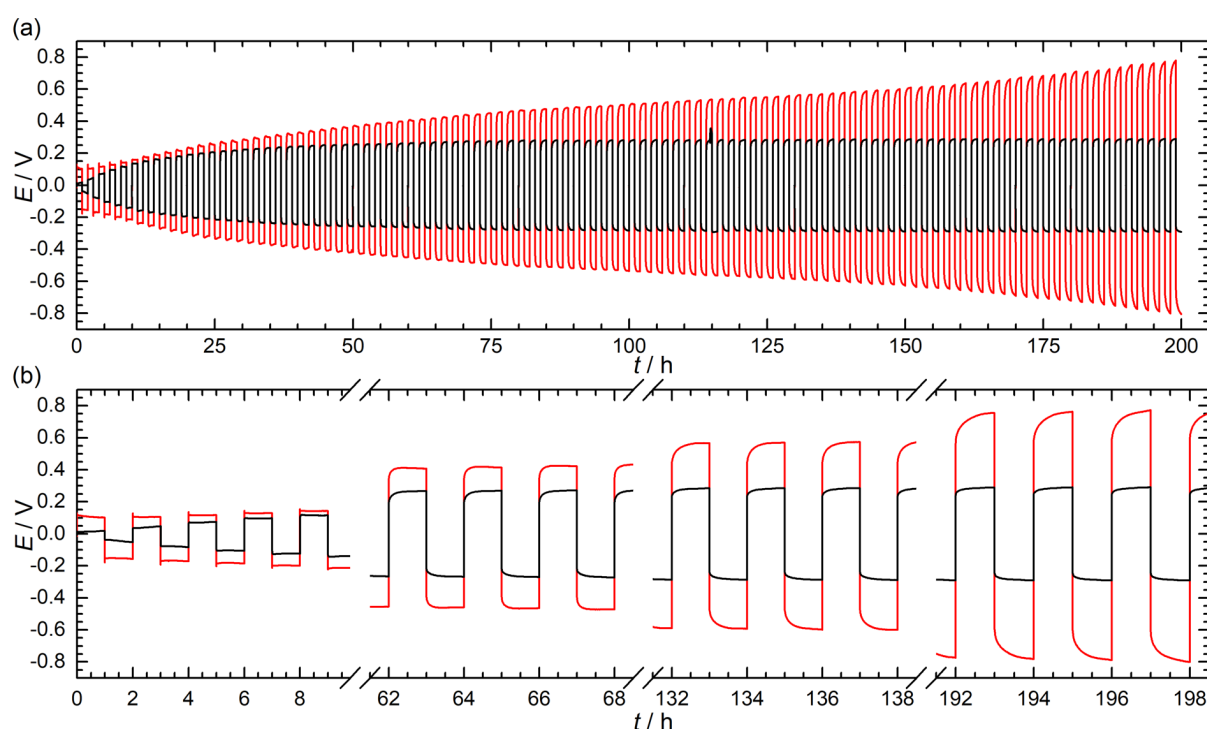

Figure 9: Galvanostatic plating and stripping experiments in symmetric Li|SE|Li cells obtained at 323 K at ±0.01 mA cm^{-2} for 1 h (0.01 mAh cm^{-2}) per half-cycle. (a) overview for $Li_{4.4}Al_{0.4}Ge_{0.6}S_4$ (black) and $Li_{4.4}Al_{0.4}Sn_{0.6}S_4$ (red), (b) enlarged voltage profiles for selected time intervals.

3.2.3 NMR Structure: ^6Li, ^{27}Al and ^{119}Sn

^6Li MAS NMR spectra measured at room temperature for $Li_{4.4}Al_{0.4}Ge_{0.6}S_4$ and $Li_{4.4}Al_{0.4}Sn_{0.6}S_4$ are presented in Figure 10 (a). The ^6Li NMR spectrum of $Li_{4.4}Al_{0.4}Sn_{0.6}S_4$ displays three overlapping resonances in agreement with the existence of three distinct Li sites in its crystal structure (Figure S12). A sharp peak at ~1.1 ppm, a broad resonance at ~1.1 ppm and a shoulder at ~1.3 ppm in a 1.3(1):1:1.1(1) ratio are observed and respectively assigned to the tetrahedral Li1, Li2 and square-pyramidal Li3 based on the 1.4:1:1.1 ratio obtained from the sites occupancy at room temperature (Table 1). Although $Li_{4.4}Al_{0.4}Ge_{0.6}S_4$ and $Li_{4.4}Al_{0.4}Sn_{0.6}S_4$ are isostructural, the ^6Li NMR spectrum of the former phase only shows a single narrow peak at ~1.2 ppm (with a full width at half maximum fwhm of ~30 Hz). It is likely that this arises from fast motional narrowing on the NMR time scale at room temperature of the ^6Li NMR resonances due to the higher Li^+ conductivity of $Li_{4.4}Al_{0.4}Ge_{0.6}S_4$ vs $Li_{4.4}Al_{0.4}Sn_{0.6}S_4$ as revealed by the AC impedance data, preventing the resolution of the three individual Li1, Li2, and Li3 sites. Note that the low-level lithium-containing impurities identified by SXRD (Figure S4 and Table 2) are not observed clearly in the NMR spectra of either compound, due

to a combination of their small phase fractions (<1 mol%) and the limited range of the [6]Li chemical shifts.[45]

The room temperature ^{27}Al MAS NMR spectra of $Li_{4.4}Al_{0.4}Ge_{0.6}S_4$ and $Li_{4.4}Al_{0.4}Sn_{0.6}S_4$ are given in Figure 10 (b). Both spectra are dominated by a resonance with an isotropic chemical shift at ~130 ppm attributed to AlS_4 tetrahedra based on known literature values for this environment[46] and in agreement with the Al^{3+} occupying the tetrahedral layer of these phases (Figure 4 (a) and S10)). The two-dimensional ^{27}Al 3QMAS NMR spectrum of $Li_{4.4}Al_{0.4}Ge_{0.6}S_4$ (Figure 10 (c)) around the AlS_4 region shows the presence of two slightly different Al environments which correspond to the two partially occupied Al^{3+} sites. Note that this two dimensional experiment is not quantitative and therefore the signal intensities of the two overlapping [27]Al resonances do not necessarily match the occupancies of the Al atoms in the Al^{3+}/Ge^{4+} tetrahedral sites. A single AlS_4 peak is observed in the 3QMAS NMR spectrum of $Li_{4.4}Al_{0.4}Sn_{0.6}S_4$ and indicates that the NMR shifts and quadrupolar parameters of both Al^{3+} sites are too close to enable their resolution under the experimental condition used to acquire these data. The much smaller [27]Al signals at ~15 ppm are assigned to a small amount of corundum (α-Al_2O_3) impurity (Figure 10(b)) based on the literature value for octahedral Al in this phase.[47-48]

The room temperature ^{119}Sn MAS NMR spectrum of $Li_{4.4}Al_{0.4}Sn_{0.6}S_4$ is given in Figure S17 and shows resonances between 40 and 90 ppm in a region similar to the tetrahedral SnS_4 in $Li_{10}SnP_2S_{12}$.[49] Although a single [119]Sn resonance would be expected from the symmetrical Sn tetrahedra with identical Sn-S bond lengths (of 2.324(2) Å) and an average S-Sn-S bond angle of 109.5(1)^O, at least 6 [119]Sn signals are detected and are assigned to short range ordering of Li and Al.
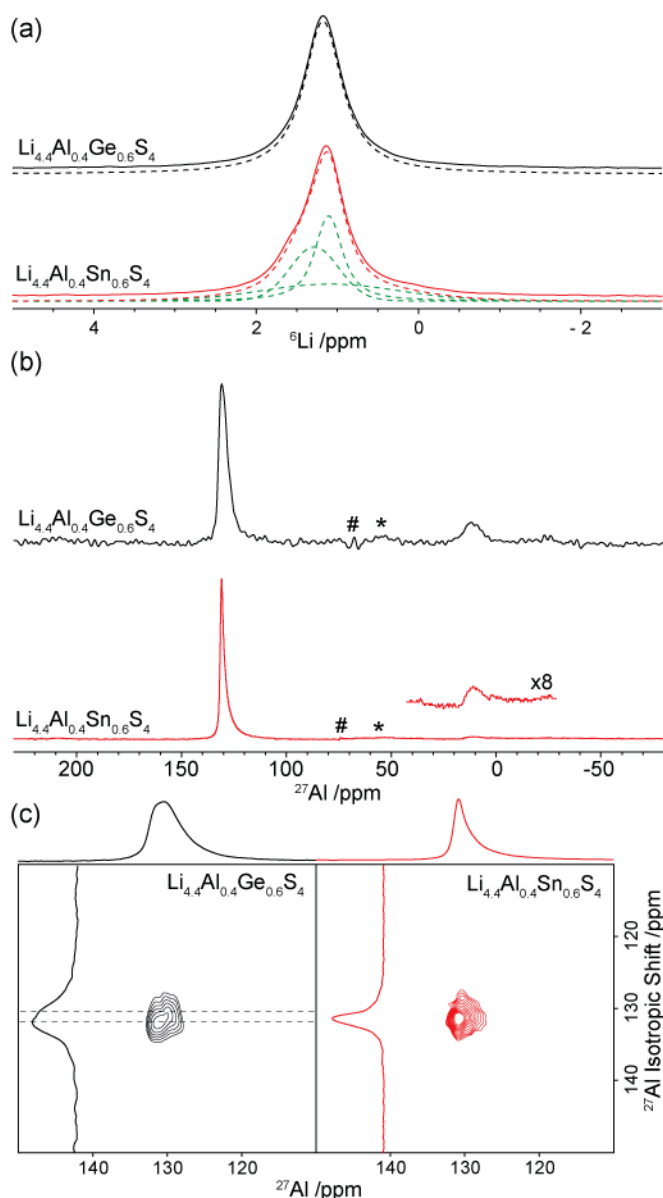
Figure 10: (a) ^6Li MAS NMR spectra of $Li_{4.4}Al_{0.4}Ge_{0.6}S_4$ (black) (synthesised using commercial Li_2S and Ge) and $Li_{4.4}Al_{0.4}Sn_{0.6}S_4$ (red) (synthesised purified reagents) at MAS rate of v_r = 10 kHz. The black dotted line represent a single line shape simulation. Red dotted lines represent the sum of simulated peaks (green dotted lines). (b) ^{27}Al MAS NMR spectra. The small peak at ~15 ppm corresponds to a small amount of α-Al_2O_3 impurity. The experimental value of ~2.4(1) wt% of Al_2O_3 in the sample obtained by NMR is consistent with the value of 2.2 wt% observed in SXRD analysis (Figure S4). A very small amount of α-Al_2O_3 (see insert) is also seen in $Li_{4.4}Al_{0.4}Sn_{0.6}S_4$ that was not observed in PXRD (Figure S18). (c) ^{27}Al 3QMAS NMR of $Li_{4.4}Al_{0.4}Ge_{0.6}S_4$ and $Li_{4.4}Al_{0.4}Sn_{0.6}S_4$ at MAS frequency of v_r = 8 kHz. Top spectra: 30° flip angle MAS NMR spectra. Asterisks (*) denote spinning sidebands. Hash sign (#) denote centre spike from carrier frequency.

3.2.4 NMR Dynamics: Line narrowing

The temperature dependences of the ^7Li static NMR spectra of $Li_{4.4}Al_{0.4}Ge_{0.6}S_4$ and $Li_{4.4}Al_{0.4}Sn_{0.6}S_4$ are shown in Figure 11 (a-b). In static ^7Li (spin 3/2) NMR spectra of Li-containing materials and in the absence of Li$^+$ mobility, the 1/2$\leftrightarrow$-1/2 central transition is usually broadened in the kHz regime by the ^7Li-^7Li homonuclear dipolar interactions as seen at 121 K here where fwhm of ~5.5 kHz are obtained. The same fwhm is indeed expected for both materials as the density of ^7Li spins is identical in isostructural $Li_{4.4}Al_{0.4}Ge_{0.6}S_4$ and $Li_{4.4}Al_{0.4}Sn_{0.6}S_4$ phases. Upon heating, line narrowing of the central

22

transition is observed and this results from an averaging to zero of the ^{7}Li dipolar coupling interaction indicative of increasing Li$^+$ mobility. At 411K for Li$_{4.4}$Al$_{0.4}$Ge$_{0.6}$S$_4$ and 538 K for Li$_{4.4}$Al$_{0.4}$Sn$_{0.6}$S$_4$, the NMR spectra show the expected line shape from a spin 3/2 nucleus, with broad shoulders on either side of the central transition arising from the 3/2↔1/2 and -3/2↔-1/2 satellite transitions that permit the determination of quadrupolar coupling constants of ~15-17 kHz.
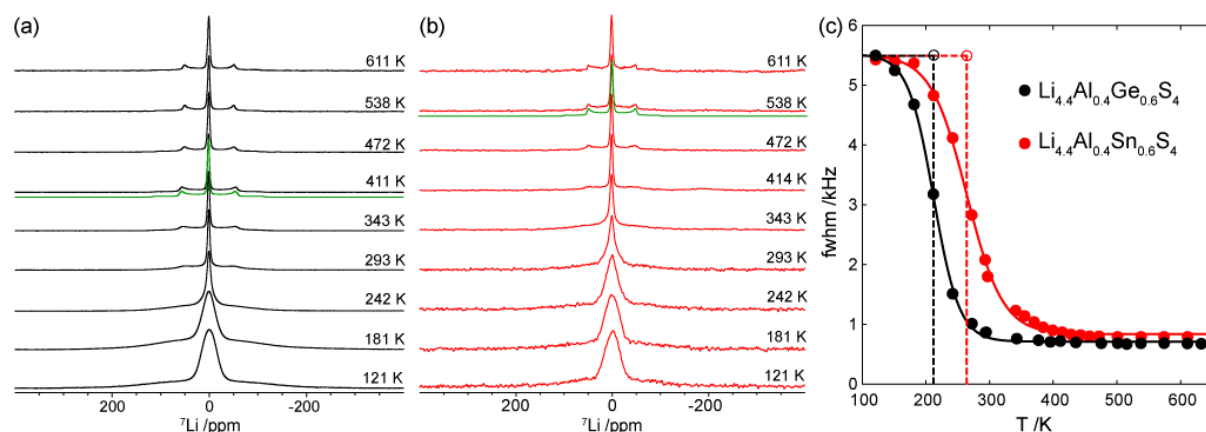

Figure 11: ^{7}Li NMR spectra as a function of temperature for (a) Li$_{4.4}$Al$_{0.4}$Ge$_{0.6}$S$_4$ and (b) Li$_{4.4}$Al$_{0.4}$Sn$_{0.6}$S$_4$. The green spectra are the line shape simulations of a single Li environment with quadrupole coupling constants C$_Q$ of ~17 kHz (for Li$_{4.4}$Al$_{0.4}$Ge$_{0.6}$S$_4$) and ~15 kHz (for Li$_{4.4}$Al$_{0.4}$Sn$_{0.6}$S$_4$) with null asymmetry parameters η. (c) Temperature dependence of ^{7}NMR line width of Li$_{4.4}$Al$_{0.4}$Ge$_{0.6}$S$_4$ (black) and Li$_{4.4}$Al$_{0.4}$Sn$_{0.6}$S$_4$ (red) fitted with sigmoidal regression curve (solid lines). The vertical and horizontal dashed lines give the temperatures corresponding to the inflection point of the regression curve and the NMR line width used to determine the Li$^+$ jump rates τ^{-1}, respectively.

The room temperature ^{7}Li central transition of the static NMR spectrum of Li$_{4.4}$Al$_{0.4}$Sn$_{0.6}$S$_4$ is much broader than that of Li$_{4.4}$Al$_{0.4}$Ge$_{0.6}$S$_4$ (fwhm ~2 kHz vs ~860 Hz), demonstrating that Li$^+$ ions in the latter phase are in the fast motion regime and more mobile than in Li$_{4.4}$Al$_{0.4}$Ge$_{0.6}$S$_4$ in agreement with the conductivity data. This could also be quantified in Figure 11 (c) by comparing the temperature dependence of the ^{7}Li central transition NMR line widths for both Li$_{4.4}$Al$_{0.4}$Ge$_{0.6}$S$_4$ and Li$_{4.4}$Al$_{0.4}$Sn$_{0.6}$S$_4$. The inflection point of this regression curve defines the Li$^+$ jump rates τ^{-1}, which are of the order of the central transition NMR line width in the rigid lattice regime (fwhm ~ 5.5 kHz), yielding values of ~3.5 x 10^4 s^{-1} at 212(10) and 264(5) K for Li$_{4.4}$Al$_{0.4}$Ge$_{0.6}$S$_4$ and Li$_{4.4}$Al$_{0.4}$Sn$_{0.6}$S$_4$, respectively. The onset of motional narrowing therefore occurs at a lower temperature for the Ge phase than for the Sn one indicating faster Li$^+$ ion dynamics in the former phase.

3.2.5 NMR Dynamics: Relaxometry

Further information on Li$^+$ dynamics on the MHz and kHz timescale were obtained by monitoring the temperature dependence of the ^{7}Li spin-lattice relaxation rates (SLR) in the laboratory frame (T$_1$$^{-1}$) and rotating frame (T$_{1\rho}$$^{-1}$) under static conditions (Figure 12). Upon heating, the SLR T$_1$$^{-1}$ values for both Li$_{4.4}$Al$_{0.4}$Ge$_{0.6}$S$_4$ and Li$_{4.4}$Al$_{0.4}$Sn$_{0.6}$S$_4$ materials increase with temperature with an activation barrier of 0.19(2) eV below room temperature and 0.11(1) eV above room temperature for Li$_{4.4}$Al$_{0.4}$Ge$_{0.6}$S$_4$ (blue circles in Figure 12 (a)) and 0.26(3) eV above 250 K for Li$_{4.4}$Al$_{0.4}$Sn$_{0.6}$S$_4$ (red circles in Figure 12 (b)), and are indicative of the slow motion regime (where ω$_0$τ$_c$ >> 1, where ω$_0$ is the Larmor frequency and τ$_c$ is the correlation time of Li motion), characterising local hopping processes between local energy minima and unsuccessful jumps to the neighbouring sites.

In $Li_{4.4}Al_{0.4}Ge_{0.6}S_4$, the SLR $T_{1\rho}^{-1}$ values increase with temperature between 200 K and room temperature with an activation barrier of 0.12(1) eV and suggests that this hopping process occurring in the ms time scale is similar to the one observed in the ns time scale in the SLR T_1^{-1} data above. In $Li_{4.4}Al_{0.4}Sn_{0.6}S_4$, the SLR $T_{1\rho}^{-1}$ values measured up to 370 K give an activation barrier of 0.18(1) eV and describe a much slower diffusion process that the one probed in the T_1^{-1} data. Note that the $T_{1\rho}^{-1}$ values for $Li_{4.4}Al_{0.4}Sn_{0.6}S_4$ are larger than the ones obtained for $Li_{4.4}Al_{0.4}Ge_{0.6}S_4$, highlighting the more favourable hopping process found with the Ge phase. The fast motional regime characterised by $\omega_1\tau_c << 1$ (where ω_1 is the spin-lock frequency) and corresponding translational diffusion of Li^+ ions evidenced by $T_{1\rho}^{-1}$ values decreasing with increasing temperatures is observed above 320 and 414 K for $Li_{4.4}Al_{0.4}Ge_{0.6}S_4$ and $Li_{4.4}Al_{0.4}Sn_{0.6}S_4$, respectively (Figure 12 (a-b)). The lower temperature of these $T_{1\rho}^{-1}$ maxima for the Ge phase show that the Li^+ ions are more mobile in this phase than in the Sn phase. This is also associated with a smaller activation barrier for Li^+ hopping of 0.22(4) eV for $Li_{4.4}Al_{0.4}Ge_{0.6}S_4$ and 0.34(1) eV for $Li_{4.4}Al_{0.4}Sn_{0.6}S_4$.

$T_{1\rho}^{-1}$ maxima are observed where Li^+ ion jump rates τ^{-1} are on the order of the probe frequency ω_1 and followed the following equation $2\omega_1\tau_c \approx 1$.[50] Jump rates in the order of 2–7 x 10^5 s^{-1} in the 280-320 K and 370-420 K temperature range for $Li_{4.4}Al_{0.4}Ge_{0.6}S_4$ and $Li_{4.4}Al_{0.4}Sn_{0.6}S_4$, respectively, are therefore obtained.
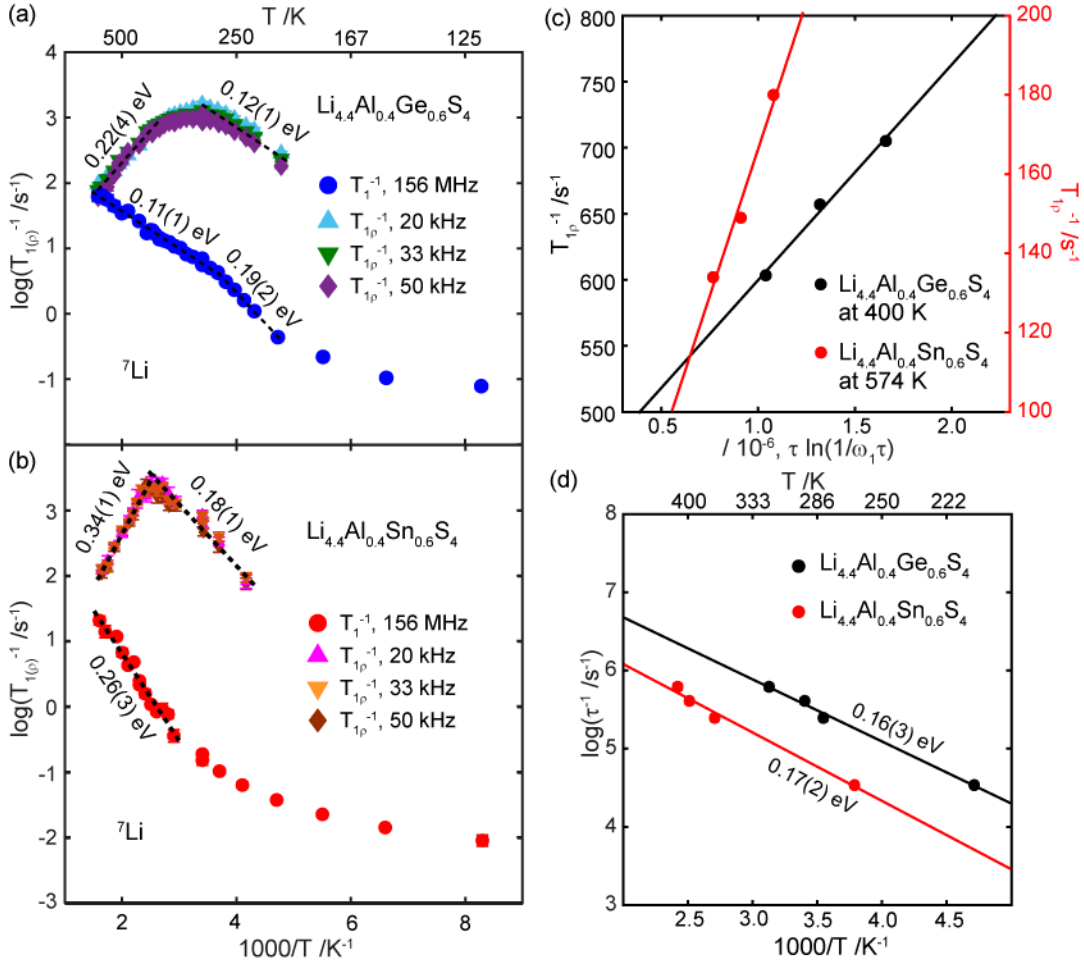
Figure 12: Arrhenius plot of spin-lattice relaxation (SLR) rates in the laboratory frame (T_1^{-1}) and the rotating frame ($T_{1\rho}^{-1}$) for (a) $Li_{4.4}Al_{0.4}Ge_{0.6}S_4$ and (b) $Li_{4.4}Al_{0.4}Sn_{0.6}S_4$. The black dotted lines represent the temperature range where the activation energy E_a is determined. (c) Frequency dependence of $T_{1\rho}^{-1}$ for $Li_{4.4}Al_{0.4}Ge_{0.6}S_4$ (black) and $Li_{4.4}Al_{0.4}Sn_{0.6}S_4$ (red). (d) Arrhenius plot of Li^+ jump rates τ^{-1} extracted from ^7Li line width analysis and SLR experiments for $Li_{4.4}Al_{0.4}Ge_{0.6}S_4$ (black) and $Li_{4.4}Al_{0.4}Sn_{0.6}S_4$ (red). A zoomed in view of the $T_{1\rho}^{-1}$ maximum and the high temperature flank is available in the SI (Figure S19).

The dimensionality of the Li^+ ion diffusion can be accessed from the frequency-dependence of the high temperature limits of the SLR $T_{1\rho}^{-1}$ values with one, two and three dimensional diffusion in solids being proportional to $(\tau/\omega)^{0.5}$, $\tau \ln(1/\omega\tau)$ or τ, respectively (where τ and ω are the correlation times and probe frequencies).[51-52] A plot of $T_{1\rho}^{-1}$ values against $\tau \ln(1/\omega\tau)$ at 400 K for $Li_{4.4}Al_{0.4}Ge_{0.6}S_4$ and at 574 K for $Li_{4.4}Al_{0.4}Sn_{0.6}S_4$ (Figure 12 (c)), which are in the fast motion regime for the respective samples, reveals a clear linear trend, demonstrating two dimensional lithium diffusion in this family of materials.

The Bloembergen-Purcell-Pound (BPP) theory of relaxation predicts a quadratic dependence of the SLRs with the probe frequency (i.e. $T_{1\rho}^{-1} \alpha \omega^{-\beta}$ with $\beta = 2$), however this is often not the case in fast Li^+ ion conductors.[51] This results in an asymmetric behaviour of $T_{1\rho}^{-1}$ rates in the fast and slow motional regimes, as indeed observed for both $Li_{4.4}Al_{0.4}Ge_{0.6}S_4$ and $Li_{4.4}Al_{0.4}Sn_{0.6}S_4$ (Figure 12 (a-b)), and arises from local interactions including repulsive Coulomb interactions and structural disorder. The deviation from BPP can be characterised from a correlation factor β which is determined by $E_{a,low} = E_{a,high}(\beta - 1)$, where $E_{a,low}$ and $E_{a,high}$ are the activation barriers in the slow and fast motion regimes,

respectively; here similar β values were obtained for $Li_{4.4}Al_{0.4}Ge_{0.6}S_4$ ($\beta(Li_{4.4}Al_{0.4}Ge_{0.6}S_4) \approx 1.55$) and $Li_{4.4}Al_{0.4}Sn_{0.6}S_4$ ($\beta(Li_{4.4}Al_{0.4}Sn_{0.6}S_4) \approx 1.53$) also suggesting a similar Li^+ diffusion pathway.

NMR-derived jump rates τ^{-1} from NMR line narrowing experiments and relaxometry experiments are plotted against reciprocal temperature in Figure 12 (d). Fitting to $\tau^{-1} = \tau_0^{-1} \exp(-E_a/RT)$ yields activation barriers of 0.16(3) and 0.17(2) eV and pre-exponential factors τ_0^{-1} of $1.9(1.4) \times 10^8$ and $6.8(2.7) \times 10^7$ s^{-1} for $Li_{4.4}Al_{0.4}Ge_{0.6}S_4$ and $Li_{4.4}Al_{0.4}Sn_{0.6}S_4$, respectively. The activation barrier for $Li_{4.4}Al_{0.4}Ge_{0.6}S_4$ is within error of the value extracted from the high temperature flank of the relaxometry plot (0.22(4) eV), suggesting the same two dimensional Li^+ diffusion process in the line narrowing and relaxometry experiments. However, in the case of $Li_{4.4}Al_{0.4}Sn_{0.6}S_4$, the activation barrier of 0.17(2) eV is not within the range of the long range Li^+ diffusion of the $T_{1\rho}^{-1}$ rates (0.34(1) eV, Figure 12 (b)) and suggests that a much slower dynamics process than two dimensional diffusion is also present, explaining the lower conductivity of this phase compared to $Li_{4.4}Al_{0.4}Ge_{0.6}S_4$.

NMR conductivity σ_{NMR} can be estimated from the Li^+ jump rates τ^{-1} using the combined Nernst-Einstein and Einstein-Smoluchowski equations:

$$\sigma = \frac{f}{H_R} \frac{N_{CC}q^2a^2}{N_{NN}k_BT} \frac{1}{\tau} \tag{1}$$

where f/H_R is the correlation factor and Haven ratio (1 for uncorrelated motion), N_{CC} is the number of charge carriers per unit cell volume (335.5(2)-337.8(2) $Å^3$ for $Li_{4.4}Al_{0.4}Ge_{0.6}S_4$ and 349.6(2)-352.9(2) $Å^3$ for $Li_{4.4}Al_{0.4}Sn_{0.6}S_4$ in this temperature range, see Figure S20), q is the ionic charge of Li^+, a is the closest Li3–Li3 jump distance at room temperature (3.6(1) Å for $Li_{4.4}Al_{0.4}Ge_{0.6}S_4$ and $Li_{4.4}Al_{0.4}Sn_{0.6}S_4$), N_{NN} is the number of neighbouring Li sites (4 for the two dimensional diffusion here).[53] The extrapolated conductivity values at 303 K for $Li_{4.4}Al_{0.4}Ge_{0.6}S_4$ and $Li_{4.4}Al_{0.4}Sn_{0.6}S_4$ are 1.9(1) $\times 10^{-5}$ S cm^{-1} and 3.6(4) $\times 10^{-6}$ S cm^{-1} respectively (see Figure S21), which are in good agreement with the values determined by impedance spectroscopy. The NMR activation barriers obtained (0.14(2) and 0.15(3) eV for $Li_{4.4}Al_{0.4}Ge_{0.6}S_4$ and $Li_{4.4}Al_{0.4}Sn_{0.6}S_4$, respectively) are significantly lower than those observed by impedance spectroscopy (Table 3), as NMR spectroscopy determines the barrier of diffusion of Li to its neighbouring site, whereas impedance measurements probe longer range translational Li^+ diffusion.[54-59]

3.2.6 Ab initio molecular dynamics
Ab initio molecular dynamics (AIMD) calculations were performed for two configurations of atoms in (**a**−**b**, 2**a**+3**b**, 2**c**) supercells of $Li_{4.4}Al_{0.4}Ge_{0.6}S_4$ (where **a**, **b** and **c** describe the experimentally determined unit cell), with overall composition $Li_{88}Al_8Ge_{12}S_{80}$. These two configurations, henceforth labelled supercells A and B, were chosen as low energy configurations from a screen of 100 different configurations in the same sized supercell (see Experimental Section).

Close inspection of the Li^+ ion trajectories during AIMD (Figure 13, Figures S22-S23) reveal a qualitative description of Li^+ ion dynamics at 400 K. No transport of Li^+ ions is observed across the tetrahedral layer containing Li1, Al and Ge ions (Figure 13**Error! Reference source not found.** (d)). This is in excellent agreement with the linear frequency dependence of the high temperature slope of the ^7Li $T_{1\rho}^{-1}$ SLR (Figure 12 (c)), which experimentally demonstrates two dimensional Li^+ ion motion.
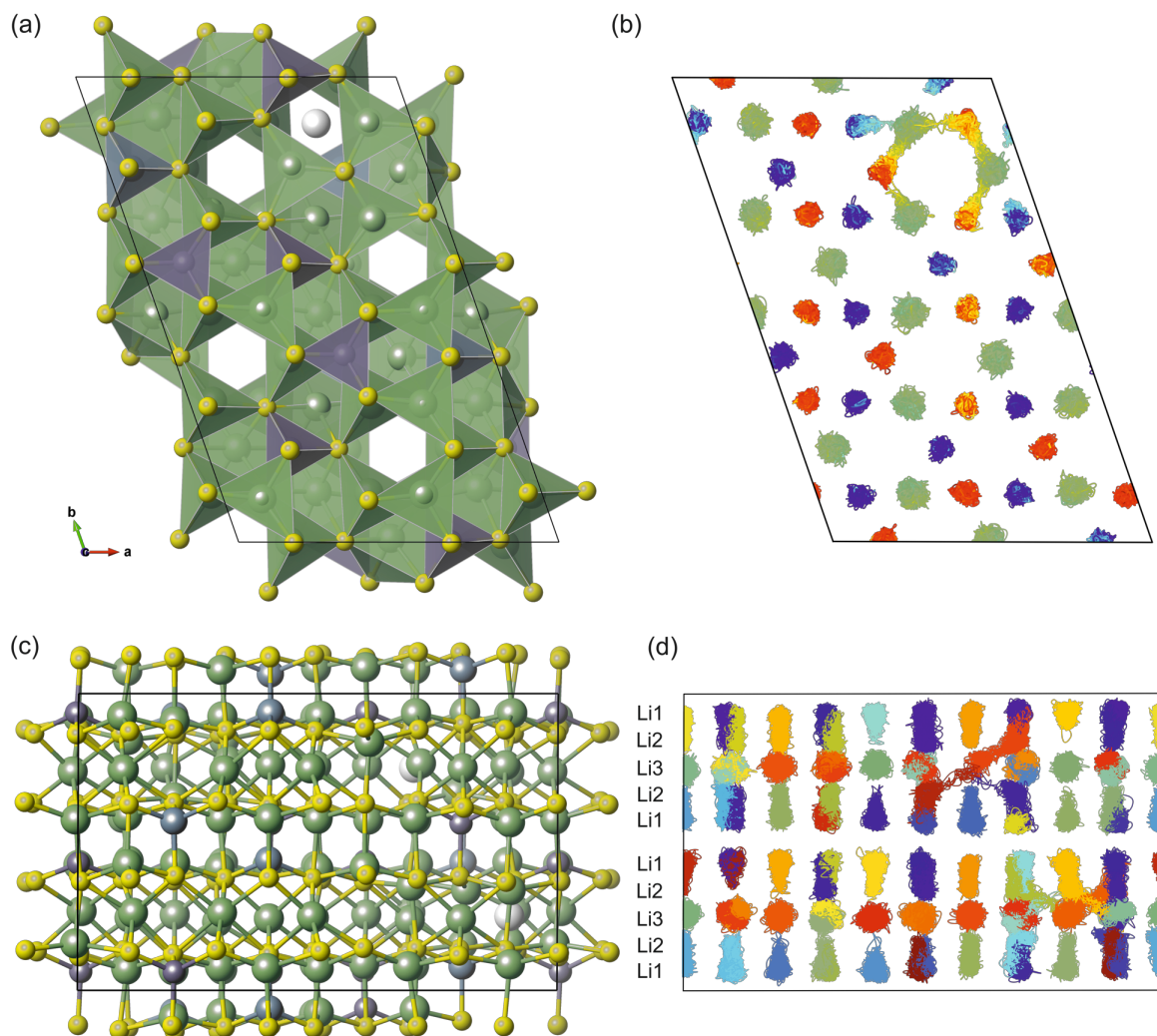
Figure 13: The AIMD trajectory of Li ions in supercell A. (a) shows the view down the c axis of bottom half of supercell A before the AIMD trajectory begins (yellow: sulfur, green: lithium, blue: aluminium and purple: germanium), with the initially vacant Li3 site shown as a grey sphere. (b) shows the Li ion positions in this bottom half of the cell throughout the 88 ps AIMD trajectory. Atoms are coloured according to position along c, with (pseudo)octahedral sites in green, and tetrahedral sites in blues and reds. (c) shows a view down the a axis of supercell A before the AIMD trajectory begins. (d) shows the Li ion positions viewed down the same axis throughout the 88 ps AIMD trajectory with each atom's positions shown in a different colour.

At a local level, hopping between the two face-sharing tetrahedral sites (Li1 in the tetrahedral layer and Li2 in the octahedral layer) is rapid at 400 K (Figure 13 (d)). In Figure 14 (c), we show the free energy as a function of distance along the c axis for supercells A and B, considering the top and bottom halves of each supercell separately. We observe a larger free energy barrier of 0.055 ± 0.004 eV for hopping from Li1 to Li2 sites, and a smaller barrier of 0.009 ± 0.002 eV for hopping from Li2 to Li1 sites. These are relatively low energy hopping processes, resulting in the rapid exchange between these face-sharing tetrahedral sites observed in AIMD.

No Li$^+$ ions are observed to occupy the ordered vacancies in the octahedral layer, which do not appear to participate in Li$^+$ ion transport at this temperature. However, longer range Li$^+$ ion transport is mediated by the disordered vacancies in Li3 octahedral interstices. Li$^+$ ions are observed to hop from neighbouring Li2 tetrahedral sites into these disordered vacant Li3 sites, leaving behind a vacant Li2 tetrahedral site (Figure 14 (a)). This can be filled by reversing the original hopping process, leaving the same Li3 site unoccupied, or alternatively, the vacant Li2 site can be filled by hopping from a different neighbouring Li3 site, leaving that site unoccupied, and effectively migrating the Li$^+$ ion vacancy from one Li3 site to a neighbouring Li3 site via a vacant Li2 intermediate. To determine the energy barrier for moving an atom from the Li2 tetrahedral site to the Li3 square pyramidal vacancy we have run nudged elastic band calculations for one such vacancy in supercell A (Figure 14 (b)). We find that the energy barrier for this vacancy hopping event is 0.17 eV. This is experimentally verified in the Arrhenius plot of the Li$^+$ ion jump rates obtained from ^{7}Li NMR data which revealed the same activation barrier of 0.16(3) eV (Figure 12 (d)).
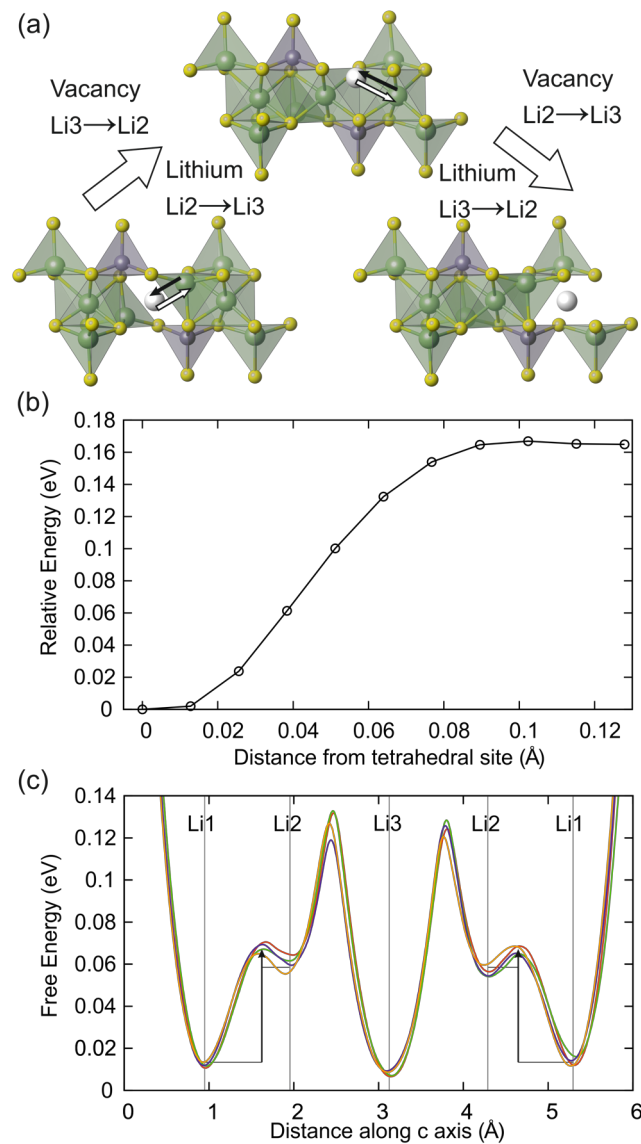
Figure 14: (a) A schematic representation of longer range Li$^+$ ion transport between Li2 sites via the disordered vacancy in a Li3 site. The Li$^+$ ion in a Li2 site hops into the Li3 vacancy, and the now vacant Li2 site is filled by a Li$^+$ ion from a Li3 site. (b) The relative energy of the structure is shown as a Li2 ion moves into a Li3 vacancy in supercell A. (c) The free energy of Li$^+$ ions as a function of the distance along the c axis in supercells A and B,

The bottom half of supercell A is shown in red, with the top half in green. For supercell B, the bottom half is shown in blue, and the top half in orange. Barriers to Li1–Li2 transitions are indicated using arrows.

These vacancy hopping events are rare on the timescale probed by AIMD but will combine resulting in long-range two dimensional transport through the crystal. In 120 ps, 12 of these Li3-Li3 hopping events were observed over the two supercells, containing in total 176 Li$^+$ ions. This gives an estimated hopping rate τ^{-1} at 400 K of 5.7×10^8 s^{-1} per Li$^+$ ion. Using this value in the combined Nernst-Einstein and Einstein-Smoluchowski equations (equation 1 in section 3.2.5) with the volume of the cell at 400 K (339.6 Å^3) and the Li3–Li3 distance at room temperature (a = 3.6 Å) yields a conductivity of σ_{MD} of 2.2×10^{-2} S·cm^{-1} at 400 K. This is 1-2 orders of magnitude greater than that measured by AC impedance spectroscopy and obtained by variable temperature ^{7}Li NMR experiments. The overestimate is likely to be the result of AC impedance spectroscopy reporting total rather than pure bulk conductivity, the NMR probing long range translational diffusion and the poor statistics in AIMD where only 12 hopping events are observed.

The Site Displacement Function (SDF) was computed to evaluate the occupancy of octahedral interstices as a function of time[60] with a radial cutoff, r_{cut}, of 1.5 Å. The SDF is zero if an atom is further than r_{cut} from a given crystallographic site, and takes the value of $(r_{cut}-r_{ij})/r_{cut}$ otherwise, where r_{ij} is the distance of atom j away from site i. The results for all octahedral Li3 interstices are shown in Figures S24-S25. Most octahedral Li3 sites remain fully occupied through the full AIMD trajectory, however site hopping is observed in octahedral sites which are initially vacant, and in their immediate neighbours. An example of site hopping is shown Figure 15 for the AIMD trajectory of three neighbouring octahedral sites in supercell A.
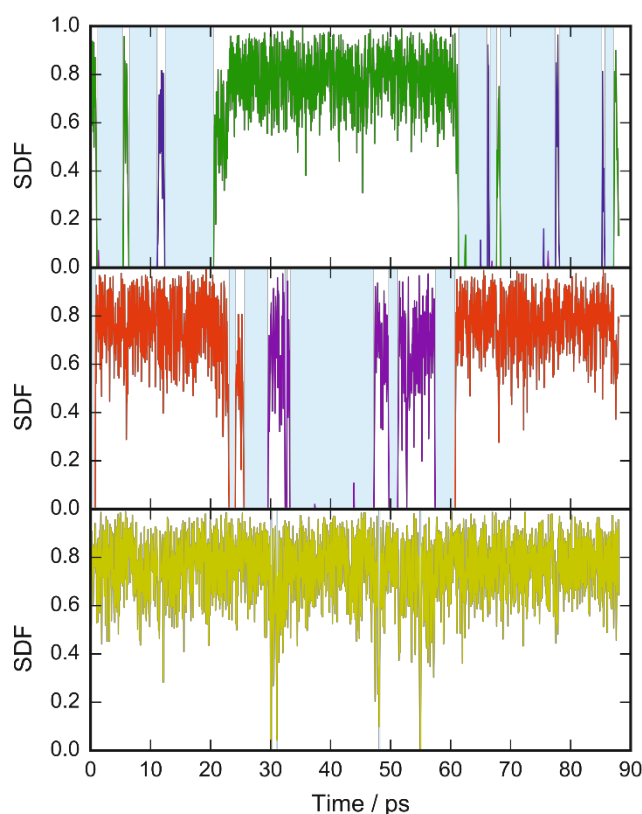

Figure 15: SDF plots for three octahedral sites in supercell A as a function of time. A value of zero in the SDF means that the site is vacant, and a value of one that the Li atom is at the centre of the octahedral site. Different coloured lines represent

different Li atoms in the AIMD calculation. Pale blue shading indicates periods of time when the vacancy resided in the octahedral site. The vacancy moves between different octahedral sites, though it spends very little time in the site at the bottom of the plot which remains vacant for fractions of 1 ps. At times when all three octahedra are occupied, the vacancy resides in a neighbouring tetrahedral site.

The two dimensional Li^+ ion motion computed and observed experimentally in $Li_{4.4}Al_{0.4}M'_{0.6}S_4$ ($M'=$ Ge^{4+}, Sn^{4+}) is mediated by vacancies in both the tetrahedral and octahedral layers (Figure 4 (a) and Figure 5). The ionic conductivity of $Li_{4.4}Al_{0.4}M'_{0.6}S_4$ is likely reduced however by the low concentration of vacant sites, leading to low carrier concentrations, and the presence of ordered vacancies which do not participate in Li^+ transport, reducing the number of possible hopping pathways through the material.

The two dimensional diffusion process identified by NMR is consistent with the layered structures of $Li_{4.4}Al_{0.4}Ge_{0.6}S_4$ and $Li_{4.4}Al_{0.4}Sn_{0.6}S_4$ obtained by neutron diffraction, with the tetrahedral layer providing a barrier to significant Li^+ diffusion along the c axis, despite the availability of vacant octahedral interstices in this layer. One possible explanation is the full occupation of Li1/Li2 pairs: hopping across the tetrahedral layer (i.e. from Li1 to Li1) would produce simultaneous occupation of Li1 and Li2 locally, which is strongly disfavoured electrostatically; a secondary factor may be that three-quarters of these vacant octahedral interstices share faces with highly charged (Al^{3+}/Ge^{4+}) tetrahedra, further disfavouring Li^+ occupancy. Li^+ ion transport is instead confined within two dimensions, centred on the octahedral layers: AIMD revealed that the prevalence of face-sharing polyhedra at the interface between the tetrahedral and octahedral layers, and the high degree of occupancy disorder, allows dynamic exchange between tetrahedral Li1 and Li2 sites which is coupled to facile diffusion between Li2 and octahedral Li3 sites within the same layer, to produce long-range two-dimensional diffusion involving all of the Li atoms in the structure. The difference in conductivity between the Ge and Sn compounds suggests that long-range diffusion is sensitive to a combination of the vacancy concentration at the partially occupied tetrahedral (Li2) sites in the octahedral layer and the packing density of the sulfide sublattice, but these factors cannot be deconvoluted without further detailed study of the variation of conductivity with composition. More generally, the comparison of the structures and properties of $Li_{4.4}Al_{0.4}M_{0.6}S_4$ with those of the ordered parent phases (e.g. Li_4GeS_4 and Li_5AlS_4) strongly suggests that the presence of multiple disordered partially-occupied lithium sites is an important factor in the realisation of high Li^+ mobilities in hcp sulfides, but extensive comparisons with other Li-rich hcp sulfides are limited by uncertainty in the precise Li arrangements in related compounds (e.g. the structure of Li_4SnS_4, where ordered[19] and disordered[43] variants have both been reported from XRD studies, is not fully understood). A complete understanding will only be made possible by precise knowledge of lithium atomic coordinates and occupancies across the whole family of materials.

4. CONCLUSIONS

A new family of isostructural lithium-rich metal sulfides $Li_{4.4}M_{0.4}M'_{0.6}S_4$ was isolated from the tie line between Li_5MS_4 and $Li_4M'S_4$ ($M= Al^{3+}$, Ga^{3+} and $M'= Ge^{4+}$, Sn^{4+}), and found to exhibit ionic conductivities in the range 4.3 x 10^{-5} – 4.2(2) x 10^{-6} S cm^{-1} at 303 K. $Li_{4.4}Al_{0.4}Ge_{0.6}S_4$ displayed good interfacial stability toward galvanostatic plating and stripping of Li, indicating that materials in this phase field could in principle function as Li^+ conducting electrolytes in solid-state batteries.

Powder neutron diffraction permitted the definitive location of the lithium sites in these solid electrolytes. Their layered crystal structures are based on a hexagonal close-packed sulfide lattice, but they have several features that distinguish them from the parent Li_5MS_4 and $Li_4M'S_4$ structures.

Firstly, the MS_4 sites are ordered in a new way within a tetrahedral layer, with the remaining tetrahedral sites in this layer only partially occupied by lithium (Li1). Secondly, they feature an octahedral layer with an ordering of octahedral site vacancies that is coupled to the MS_4 ordering in the adjacent layers; the remaining octahedral interstices in this layer are partially occupied by lithium (Li3). Finally, the "octahedral" layer hosts additional lithium ions that are disordered over three-quarters of its tetrahedral interstices (Li2). These sites share faces with the occupied octahedra, and the resulting local repulsion between Li2-Li3 causes an average displacement of Li3 from the centroid of the octahedron.

By coupling precise knowledge of the lithium distribution and occupancies from neutron diffraction to a combination of NMR measurements and AIMD calculations, we were able to connect this new structural arrangement to the transport mechanism. AIMD revealed that the ordered octahedral vacancies do not contribute to the increase in lithium mobility compared to materials with fully occupied octahedral layers (*e.g.,* Li_2FeS_2 and Li_4AlS_5). Instead, the interaction between highly disordered tetrahedral lithium sites (Li2) and their ordered pseudo-octahedral counterparts (Li3) was found to provide a two dimensional pathway for long-range diffusion, consistent with variable temperature ^{7}Li solid state NMR relaxometry data. This suggests that the charge-based control of local occupancy of octahedral and tetrahedral sites in hexagonal close packed sulfides determines the accessible lithium mobilities.

ASSOCIATED CONTENT

The Supporting Information is available free of charge on the ACS Publications website.
> Compositional analysis
> Structural parameters and partial Rietveld refinements for $Li_{4.4}Ga_{0.4}M'_{0.6}S_4$ (M'= Ge^{4+}, Sn^{4+})
> Additional AC impedance data
> Magnified view of ^{7}Li NMR relaxometry data, Arrhenius plot of NMR conductivity and [119]Sn spectrum
> Additional AIMD figures

The experimental data can be accessed from the University of Liverpool Data Catalogue portal accessible at http://dx.doi.org/10.173638/datacat.liverpool.ac.uk/522

REFERENCES

1.   Blomgren, G. E. The Development and Future of Lithium Ion Batteries. *J. Electrochem. Soc.* **2017,** *164*, A5019-A5025.

2.   Culver, S. P.; Koerver, R.; Krauskopf, T.; Zeier, W. G. Designing Ionic Conductors: The Interplay between Structural Phenomena and Interfaces in Thiophosphate-Based Solid-State Batteries. *Chem. Mater.* **2018,** *30*, 4179-4192.

3.   Sun, C.; Liu, J.; Gong, Y.; Wilkinson, D. P.; Zhang, J. Recent advances in all-solid-state rechargeable lithium batteries. *Nano Energy* **2017,** *33*, 363-386.

4.   Jiang, C.; Li, H. Q.; Wang, C. L. Recent progress in solid-state electrolytes for alkali-ion batteries. *Sci. Bull.* **2017,** *62*, 1473-1490.

5.   Ma, Z.; Xue, H. G.; Guo, S. P. Recent achievements on sulfide-type solid electrolytes: crystal structures and electrochemical performance. *J. Mater. Sci.* **2018,** *53*, 3927-3938.

6.   Meesala, Y.; Jena, A.; Chang, H.; Liu, R. S. Recent Advancements in Li-Ion Conductors for All-Solid-State Li-Ion Batteries. *ACS Energy Lett.* **2017,** *2*, 2734-2751.

7.   Zheng, F.; Kotobuki, M.; Song, S.; Lai, M. O.; Lu, L. Review on solid electrolytes for all-solid-state lithium-ion batteries. *J. Power Sources* **2018,** *389*, 198-213.

8.   Takada, K. Progress in solid electrolytes toward realizing solid-state lithium batteries. *J. Power Sources* **2018,** *394*, 74-85.

9.   Zhang, Z.; Shao, Y.; Lotsch, B. V.; Hu, Y.-S.; Li, H.; Janek, J.; Nan, C.; Nazar, L.; Maier, J.; Armand, M.; Chen, L. New Horizons for Inorganic Solid State Ion Conductors. *Energy Environ. Sci.* **2018**, Advance Article.

10.   Kamaya, N.; Homma, K.; Yamakawa, Y.; Hirayama, M.; Kanno, R.; Yonemura, M.; Kamiyama, T.; Kato, Y.; Hama, S.; Kawamoto, K.; Mitsui, A. A lithium superionic conductor. *Nat. Mater.* **2011,** *10*, 682-686.

11.   Deiseroth, H. J.; Kong, S. T.; Eckert, H.; Vannahme, J.; Reiner, C.; Zaiss, T.; Schlosser, M. Li_6PS_5X: A class of crystalline Li-rich solids with an unusually high Li^+ mobility. *Angew. Chem., Int. Edit.* **2008,** *47*, 755-758.

12.   Rayavarapu, P. R.; Sharma, N.; Peterson, V. K.; Adams, S. Variation in structure and Li^+-ion migration in argyrodite-type Li_6PS_5X (X = Cl, Br, I) solid electrolytes. *J. Solid State Electrochem.* **2012,** *16*, 1807-1813.

13.   Hayashi, A.; Noi, K.; Sakuda, A.; Tatsumisago, M. Superionic glass-ceramic electrolytes for room-temperature rechargeable sodium batteries. *Nat. Commun.* **2012,** *3*, 1-5.

14.   Wenzel, S.; Randau, S.; Leichtweiss, T.; Weber, D. A.; Sann, J.; Zeier, W. G.; Janek, J. Direct Observation of the Interfacial Instability of the Fast Ionic Conductor $Li_{10}GeP_2S_{12}$ at the Lithium Metal Anode. *Chem. Mater.* **2016,** *28*, 2400-2407.

15.   Cheng, T.; Merinov, B. V.; Morozov, S.; Goddard, W. A. Quantum Mechanics Reactive Dynamics Study of Solid Li-Electrode/Li_6PS_5Cl-Electrolyte Interface. *ACS Energy Lett.* **2017,** *2*, 1454-1459.

16.   Zhou, P. F.; Wang, J. B.; Cheng, F. Y.; Li, F. J.; Chen, J. A solid lithium superionic conductor $Li_{11}AlP_2S_{12}$ with a thio-LISICON analogous structure. *Chem. Commun.* **2016,** *52*, 6091-6094.

17.   Homma, K.; Yonemura, M.; Kobayashi, T.; Nagao, M.; Hirayama, M.; Kanno, R. Crystal structure and phase transitions of the lithium ionic conductor Li_3PS_4. *Solid State Ionics* **2011,** *182*, 53-58.

18.   Murayama, M.; Kanno, R.; Kawamoto, Y.; Kamiyama, T. Structure of the thio-LISICON, Li_4GeS_4. *Solid State Ionics* **2002,** *154-155*, 789-794.

19.   MacNeil, J. H.; Massi, D. M.; Zhang, J. H.; Rosmus, K. A.; Brunetta, C. D.; Gentile, T. A.; Aitken, J. A. Synthesis, structure, physicochemical characterization and electronic structure of thio-lithium super ionic conductors, Li_4GeS_4 and Li_4SnS_4. *J. Alloys Compd.* **2014,** *586*, 736-744.

20.   Batchelor, R. J.; Einstein, F. W. B.; Jones, C. H. W.; Fong, R.; Dahn, J. R. Crystal-Structure of Li_2FeS_2. *Phys. Rev. B* **1988,** *37*, 3699-3702.

21.   Isaenko, L.; Yelisseyev, A.; Lobanov, S.; Titov, A.; Petrov, V.; Zondy, J. J.; Krinitsin, P.; Merkulov, A.; Vedenyapin, V.; Smirnova, J. Growth and properties of $LiGaX_2$ (X = S, Se, Te) single crystals for nonlinear optical applications in the mid-IR. *Cryst. Res. Technol.* **2003,** *38*, 379-387.

22.   Lim, H.; Kim, S. C.; Kim, J.; Kim, Y. I.; Kim, S. J. Structure of Li_5AlS_4 and comparison with other lithium-containing metal sulfides. *J. Solid State Chem.* **2018,** *257*, 19-25.

23.   Murayama, M.; Kanno, R.; Irie, M.; Ito, S.; Hata, T.; Sonoyama, N.; Kawamoto, Y. Synthesis of New Lithium Ionic Conductor Thio-LISICON—Lithium Silicon Sulfides System. *J. Solid State Chem.* **2002,** *168*, 140-148.

24.   Kanno, R.; Hata, T.; Kawamoto, Y.; Irie, M. Synthesis of a new lithium ionic conductor, thio-LISICON-lithium germanium sulfide system. *Solid State Ionics* **2000,** *130*, 97-104.

25.   Johnson, D. *ZView: A Software Program for IES Analysis* 3.5d; Scribner Associates In.: 2007.

26.   Frydman, L.; Harwood, J. S. Isotropic Spectra of Half-Integer Quadrupolar Spins from Bidimensional Magic-Angle-Spinning NMR. *J. Am. Chem. Soc.* **1995,** *117*, 5367-5368.

27.   Medek, A.; Harwood, J. S.; Frydman, L. Multiple-quantum magic-angle spinning NMR: A new method for the study of quadrupolar nuclei in solids. *J. Am. Chem. Soc.* **1995,** *117*, 12779-12787.

28.   Amoureux, J. P.; Fernandez, C.; Steuernagel, S. Z filtering in MQMAS NMR. *J. Magn. Reson., Ser. A* **1996,** *123*, 116-118.

29.   Clayden, N. J.; Dobson, C. M.; Fern, A. High-resolution solid-state tin-119 nuclear magnetic resonance spectroscopy of ternary tin oxides. *J. Chem. Soc., Dalton Trans.* **1989**, 843-847.

30.   Bielecki, A.; Burum, D. P. Temperature-Dependence of [207]Pb MAS Spectra of Solid Lead Nitrate - an Accurate, Sensitive Thermometer for Variable-Temperature MAS. *J. Magn. Reson., Ser. A* **1995,** *116*, 215-220.

31.   Beckmann, P. A.; Dybowski, C. A thermometer for nonspinning solid-state NMR spectroscopy. *J. Magn. Reson.* **2000,** *146*, 379-380.

32.   Becker, K. D. Temperature-Dependence of NMR Chemical-Shifts in Cuprous Halides. *J. Chem. Phys.* **1978,** *68*, 3785-3793.

33.   Wu, J. S.; Kim, N.; Stebbins, J. F. Temperature calibration for high-temperature MAS NMR to 913 K: [63]Cu MAS NMR of CuBr and CuI, and ^{23}Na MAS NMR of $NaNbO_3$. *Solid State Nucl. Magn. Reson.* **2011,** *40*, 45-50.

34.   Kresse, G.; Furthmuller, J. Efficient iterative schemes for ab initio total-energy calculations using a plane-wave basis set. *Phys. Rev. B* **1996,** *54*, 11169-11186.

35.   Perdew, J. P.; Burke, K.; Ernzerhof, M. Generalized gradient approximation made simple. *Phys. Rev. Lett.* **1996,** *77*, 3865-3868.

36.   Kresse, G.; Joubert, D. From ultrasoft pseudopotentials to the projector augmented-wave method. *Phys. Rev. B* **1999,** *59*, 1758-1775.

37.   Toby, B. EXPGUI, a graphical user interface for GSAS. *J. Appl. Crystallogr.* **2001,** *34*, 210-213.

38.   Kwon, O.; Hirayama, M.; Suzuki, K.; Kato, Y.; Saito, T.; Yonemura, M.; Kamiyama, T.; Kanno, R. Synthesis, structure, and conduction mechanism of the lithium superionic conductor Li10+delta Ge1+delta P2-delta S12. *J Mater Chem A* **2015,** *3*, 438-446.

39.   Weber, D. A.; Senyshyn, A.; Weldert, K. S.; Wenzel, S.; Zhang, W.; Kaiser, R.; Berendts, S.; Janek, J.; Zeier, W. G. Structural Insights and 3D Diffusion Pathways within the Lithium Superionic Conductor Li10GeP2S12. *Chem. Mater.* **2016,** *28*, 5905-5915.

40.   Hori, S.; Taminato, S.; Suzuki, K.; Hirayama, M.; Kato, Y.; Kanno, R. Structure-property relationships in lithium superionic conductors having a Li10GeP2S12-type structure. *Acta Crystallogr B* **2015,** *71*, 727-736.

41.   Kraft, M. A.; Culver, S. P.; Calderon, M.; Böcher, F.; Krauskopf, T.; Senyshyn, A.; Dietrich, C.; Zevalkink, A.; Janek, J.; Zeier, W. G. Influence of Lattice Polarizability on the Ionic Conductivity in the Lithium Superionic Argyrodites Li_6PS_5X (X = Cl, Br, I). *J. Am. Chem. Soc.* **2017,** *139*, 10909-10918.

42.   Kanno, R.; Maruyama, M. Lithium ionic conductor thio-LISICON - The Li_2S-GeS_2-P_2S_5 system. *J. Electrochem. Soc.* **2001,** *148*, A742-A746.

43.   Kaib, T.; Haddadpour, S.; Kapitein, M.; Bron, P.; Schroder, C.; Eckert, H.; Roling, B.; Dehnen, S. New Lithium Chalcogenidotetrelates, LiChT: Synthesis and Characterization of the Li^+ Conducting Tetralithium ortho-Sulfidostannate Li_4SnS_4. *Chem. Mater.* **2012,** *24*, 2211-2219.

44.   Shin, B. R.; Nam, Y. J.; Oh, D. Y.; Kim, D. H.; Kim, J. W.; Jung, Y. S. Comparative Study of TiS2/Li-In All-Solid-State Lithium Batteries Using Glass-Ceramic Li3PS4 and Li10GeP2S12 Solid Electrolytes. *Electrochim Acta* **2014,** *146*, 395-402.

45.   MacKenzie, K.; Smith, M. E., *Multinuclear Solid-State Nuclear Magnetic Resonance of Inorganic Materials;*. Elsevier: Oxford, 2002.

46.   Haouas, M.; Taulelle, F.; Martineau, C. Recent advances in application of ^{27}Al NMR spectroscopy to materials science. *Prog. Nucl. Magn. Reson. Spectrosc.* **2016,** *94-95*, 11-36.

47.   Jakobsen, H. J.; Skibsted, J.; Bildsoe, H.; Nielsen, N. C. Magic-Angle Spinning NMR-Spectra of Satellite Transitions for Quadrupolar Nuclei in Solids. *J. Magn. Reson.* **1989,** *85*, 173-180.

48.   Choi, M.; Matsunaga, K.; Oba, F.; Tanakat, I. ^{27}Al NMR Chemical Shifts in Oxide Crystals: A First-Principles Study. *J. Phys. Chem. C* **2009,** *113*, 3869-3873.

49.   Kaus, M.; Stöffler, H.; Yavuz, M.; Zinkevich, T.; Knapp, M.; Ehrenberg, H.; Indris, S. Local Structures and Li Ion Dynamics in a $Li_{10}SnP_2S_{12}$-Based Composite Observed by Multinuclear Solid-State NMR Spectroscopy. *J. Phys. Chem. C* **2017,** *121*, 23370-23376.

50.   Abragam, A., *The Principles of Nuclear Magnetism*. Oxford University Press: Oxford, 1961.

51.   Heitjans, P.; Schirmer, A.; Indris, S., *NMR and β-NMR Studies of Diffusion in Interface-Dominated and Disordered Solids*. Spinger Verlag: Berlin, 2005.

52.   Kuhn, A.; Sreeraj, P.; Pottgen, R.; Wiemhofer, H. D.; Wilkening, M.; Heitjans, P. Li Ion Diffusion in the Anode Material $Li_{12}Si_7$: Ultrafast Quasi-1D Diffusion and Two Distinct Fast 3D Jump Processes Separately Revealed by ^{7}Li NMR Relaxometry. *J. Am. Chem. Soc.* **2011,** *133*, 11018-11021.

53.   Mehrer, H., *Diffusion in Solids: Fundamentals, Methods, Materials, Diffusion-Controlled Processes*. Springer-Verlag Berlin and Heidelberg GmbH & Co. KG Berlin, Germany, 2010.

54.   Enciso-Maldonado, L.; Dyer, M. S.; Jones, M. D.; Li, M.; Payne, J. L.; Pitcher, M. J.; Omir, M. K.; Claridge, J. B.; Blanc, F.; Rosseinsky, M. J. Computational Identification and Experimental Realization of Lithium Vacancy Introduction into the Olivine $LiMgPO_4$. *Chem. Mater.* **2015,** *27*, 2074-2091.

55.   Kuhn, A.; Duppel, V.; Lotsch, B. V. Tetragonal $Li_{10}GeP_2S_{12}$ and Li_7GePS_8 – exploring the Li ion dynamics in LGPS Li electrolytes. *Energy Environ. Sci.* **2013,** *6*, 3548-3552.

56.   Latie, L.; Villeneuve, G.; Conte, D.; Le Flem, G. Ionic conductivity of oxides with general formula $Li_xLn_{1/3}Nb_{1-x}Ti_xO_3$ (Ln = La, Nd). *J. Solid State Chem.* **1984,** *51*, 293-299.

57.   Deng, Y.; Eames, C.; Chotard, J.-N.; Lalère, F.; Seznec, V.; Emge, S.; Pecher, O.; Grey, C. P.; Masquelier, C.; Islam, M. S. Structural and Mechanistic Insights into Fast Lithium-Ion Conduction in Li_4SiO_4–Li_3PO_4 Solid Electrolytes. *J. Am. Chem. Soc.* **2015,** *137*, 9136-9145.

58.   Arbi, K.; Lazarraga, M. G.; Ben Hassen Chehimi, D.; Ayadi-Trabelsi, M.; Rojo, J. M.; Sanz, J. Lithium Mobility in $Li_{1.2}Ti_{1.8}R_{0.2}(PO_4)_3$ Compounds (R = Al, Ga, Sc, In) as Followed by NMR and Impedance Spectroscopy. *Chem. Mater.* **2004,** *16*, 255-262.

59.   Santibáñez-Mendieta, A. B.; Didier, C.; Inglis, K. K.; Corkett, A. J.; Pitcher, M. J.; Zanella, M.; Shin, J. F.; Daniels, L. M.; Rakhmatullin, A.; Li, M.; Dyer, M. S.; Claridge, J. B.; Blanc, F.; Rosseinsky, M. J. $La_3Li_3W_2O_{12}$: Ionic Diffusion in a Perovskite with Lithium on both A- and B-Sites. *Chem. Mater.* **2016,** *28*, 7833-7851.

60.   Noda, Y.; Nakano, K.; Takeda, H.; Kotobuki, M.; Lu, L.; Nakayama, M. Computational and Experimental Investigation of the Electrochemical Stability and Li-Ion Conduction Mechanism of $LiZr_2(PO_4)_3$. *Chem. Mater.* **2017,** *29*, 8983-8991.

TOC

2D
Li$^+$ diffusion
pathways